Article

Prediction and observation of an antiferromagnetic topological insulator

M. M. Otrokov[1,2,3,4*], I. I. Klimovskikh[4], H. Bentmann[5], D. Estyunin[4], A. Zeugner[6], Z. S. Aliev[7,8], S. Gaß[9], A. U. B. Wolter[9], A. V. Koroleva[4], A. M. Shikin[4], M. Blanco-Rey[3,10], M. Hoffmann[11], I. P. Rusinov[4,12], A. Yu. Vyazovskaya[4,12], S. V. Eremeev[4,12,13], Yu. M. Koroteev[12,13], V. M. Kuznetsov[12], F. Freyse[14], J. Sánchez-Barriga[14], I. R. Amiraslanov[7], M. B. Babanly[15], N. T. Mamedov[7], N. A. Abdullayev[7], V. N. Zverev[16], A. Alfonsov[9], V. Kataev[9], B. Büchner[9,17], E. F. Schwier[18], S. Kumar[18], A. Kimura[19], L. Petaccia[20], G. Di Santo[20], R. C. Vidal[5], S. Schatz[5], K. Kißner[5], M. Ünzelmann[5], C. H. Min[5], Simon Moser[21], T. R. F. Peixoto[5], F. Reinert[5], A. Ernst[11,22], P. M. Echenique[1,3,10], A. Isaeva[9,17] & E. V. Chulkov[1,3,4,10*]

Magnetic topological insulators are narrow-gap semiconductor materials that combine non-trivial band topology and magnetic order[1]. Unlike their nonmagnetic counterparts, magnetic topological insulators may have some of the surfaces gapped, which enables a number of exotic phenomena that have potential applications in spintronics[1], such as the quantum anomalous Hall effect[2] and chiral Majorana fermions[3]. So far, magnetic topological insulators have only been created by means of doping nonmagnetic topological insulators with 3d transition-metal elements; however, such an approach leads to strongly inhomogeneous magnetic[4] and electronic[5] properties of these materials, restricting the observation of important effects to very low temperatures[2,3]. An intrinsic magnetic topological insulator—a stoichiometric well ordered magnetic compound—could be an ideal solution to these problems, but no such material has been observed so far. Here we predict by ab initio calculations and further confirm using various experimental techniques the realization of an antiferromagnetic topological insulator in the layered van der Waals compound $MnBi_2Te_4$. The antiferromagnetic ordering that $MnBi_2Te_4$ shows makes it invariant with respect to the combination of the time-reversal and primitive-lattice translation symmetries, giving rise to a $\mathbb{Z}_2$ topological classification; $\mathbb{Z}_2 = 1$ for $MnBi_2Te_4$, confirming its topologically nontrivial nature. Our experiments indicate that the symmetry-breaking (0001) surface of $MnBi_2Te_4$ exhibits a large bandgap in the topological surface state. We expect this property to eventually enable the observation of a number of fundamental phenomena, among them quantized magnetoelectric coupling[6–8] and axion electrodynamics[9,10]. Other exotic phenomena could become accessible at much higher temperatures than those reached so far, such as the quantum anomalous Hall effect[2] and chiral Majorana fermions[3].

The first reference to $MnBi_2Te_4$ as a stable chemical compound was in 2013 when it was synthesized in the powder form[11]. The trigonal structure (space group $R\bar{3}m$) of $MnBi_2Te_4$ comprises septuple-layer blocks stacked along the [0001] direction and bound to each other by van der Waals forces (Fig. 1a). High quality $MnBi_2Te_4$ single crystals were grown at TU Dresden (hereafter, D samples; Fig. 2a) and at ASOIU Baku (B samples; Fig. 2b). Our single-crystal X-ray diffraction experiments confirm the same lattice symmetry reported previously[11]. Because the magnetism of $MnBi_2Te_4$ has not been experimentally investigated, we began our study by calculating the exchange-coupling parameters J from first principles (Fig. 1b, c). Among the intralayer interactions $J^\parallel$ the one between the nearest neighbours in the Mn layer is clearly dominant ($J_{0,1}^\parallel \approx 0.09$ meV per μ_B^2 where μ_B is the Bohr magneton), and the inter-

actions with more distant neighbours are an order of magnitude weaker, whereupon a ferromagnetic ordering is expected within each septuple-layer block of $MnBi_2Te_4$. In contrast, the interlayer coupling constants $J^\perp$ are mostly negative, resulting in a negative $J_0^\perp \approx \Sigma_{j\neq0} J_{0,j}^\perp$ coefficient equal to -0.022 meV per μ_B^2, which means that the overall coupling between neighbouring Mn layers is antiferromagnetic (AFM) (Fig. 1d). The magnetic anisotropy energy is positive and equal to 0.225 meV per Mn atom, indicating the easy axis with an out-of-plane orientation of the local magnetic moments of $\pm 4.607\mu_B$. Monte Carlo simulations confirm the interlayer AFM structure with a Néel temperature (T_N) of three-dimensional ordering of 25.4 K (Extended Data Fig. 1).

Given the magnetic ground state, the bulk electronic structure was calculated. As shown in Fig. 1f, the system is insulating, the fundamental
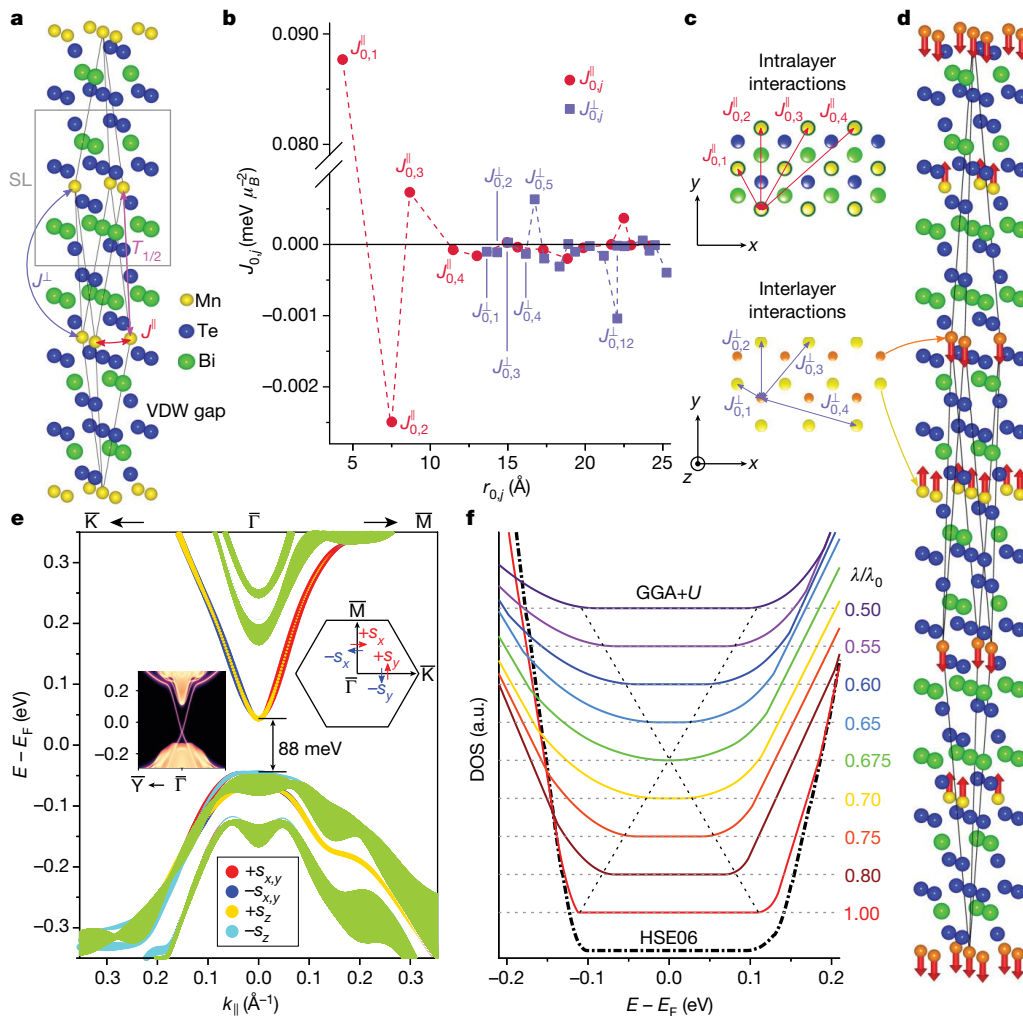
Fig. 1 | Theoretical insights into the crystal, magnetic and electronic structure of MnBi$_2$Te$_4$. a, Crystal structure of the trigonal MnBi$_2$Te$_4$ with yellow, blue and green spheres showing Mn, Te and Bi atoms, respectively. The 'nonmagnetic' rhombohedral primitive unit cell is indicated by grey lines and the $T_{1/2}$ translation is shown in magenta. VdW, van der Waals; SL, septuple layer. **b**, Calculated exchange constants $J_{0,j}$ [meV per μ_B^2] for the intralayer ($J^\parallel$, red circles) and interlayer ($J^\perp$, light blue squares) pair interactions as a function of the Mn–Mn distance, $r_{0,j}$ [Å]. **c**, Schematic top view representation of magnetic interactions in the Mn layer (top) and between two neighbouring Mn layers (bottom). **d**, Magnetic unit cell corresponding to the interlayer AFM state. The arrows on atoms denote the local magnetic moments. **e**, Spin-resolved electronic structure of the MnBi$_2$Te$_4$(0001) surface. The size of the coloured circles that comprise the data reflects the value and sign of the Cartesian projections of the spin-vector, **s**. Red and blue circles correspond to the positive and negative s_x and s_y components (perpendicular to $k_\parallel$), and yellow and cyan to the out-of-plane components $+s_z$ and $-s_z$. The green areas correspond to the bulk bandstructure projected onto the surface Brillouin zone. Left inset, The tight-binding calculated electronic bandstructure of the S-preserving (10$\bar{1}$1) surface (see also Extended Data Fig. 2). The regions with a continuous spectrum correspond to the three-dimensional bulk states projected onto the two-dimensional Brillouin zone. Right inset, the (0001) surface Brillouin zone showing the high symmetry directions along which the bandstructure shown in the main panel was calculated. Colour arrows show the Cartesian projections of the spin vector. **f**, Total DOS of bulk MnBi$_2$Te$_4$ calculated for the interlayer AFM state shown in **d** using the HSE06 exchange–correlation functional (dash-dot black line) and the GGA+U approach (solid lines). For GGA+U, the evolution of the DOS with the change of the SOC constant λ is shown (coloured lines). The thin dashed lines mark a zero DOS level for each dataset, and their intersections with the inclined lines approximately mark the bulk bandgap edges for each λ/λ_0 value. a.u., arbitrary units.

bandgap value, determined from the GGA+U calculation (the generalized gradient approximation with a Hubbard U correction for the Mn 3d states; see Methods section) of the density of states (DOS), is around 220 meV. To determine whether the gap is negative (inverted), we performed the DOS calculations decreasing the spin–orbit coupling (SOC) constant λ stepwise from its natural value λ_0 to $\lambda = 0.5\lambda_0$. It was found that at $\lambda/\lambda_0 \approx 0.675$ the gap is closed and at other values of λ/λ_0 it is non-zero, which points towards a nontrivial topology of MnBi$_2$Te$_4$.

The $\mathbb{Z}_2$ classification of AFM insulators was introduced[6] on the basis of the $S = \Theta T_{1/2}$ symmetry, which is inherent to MnBi$_2$Te$_4$ (Θ is the time-reversal symmetry and $T_{1/2}$ is the primitive lattice translation symmetry). We find $\mathbb{Z}_2 = 1$, which classifies MnBi$_2$Te$_4$ as an AFM topological insulator.

The implication of the bulk bandgap inversion in a topological insulator is seen at its surface, where the topological phase manifests itself by the appearance of the topological surface state (TSS). In the case of nonmagnetic topological insulators, this surface state is gapless[12]; however, at the (0001) surface of the AFM topological insulator MnBi$_2$Te$_4$ we find a 88-meV-wide bandgap (Fig. 1e). Here, the S symmetry is broken and the out-of-plane magnetization of the near-surface ferromagnetic layer opens the Dirac point gap[6]. In contrast, the S-preserving surface is gapless, as expected for an AFM topological insulator (inset to Fig. 1e and Extended Data Fig. 2).

Temperature- and field-dependent magnetization measurements performed on D samples (Fig. 2c, e) establish a three-dimensional AFM order below T_N = 24.2(5) K, in agreement with the prediction by
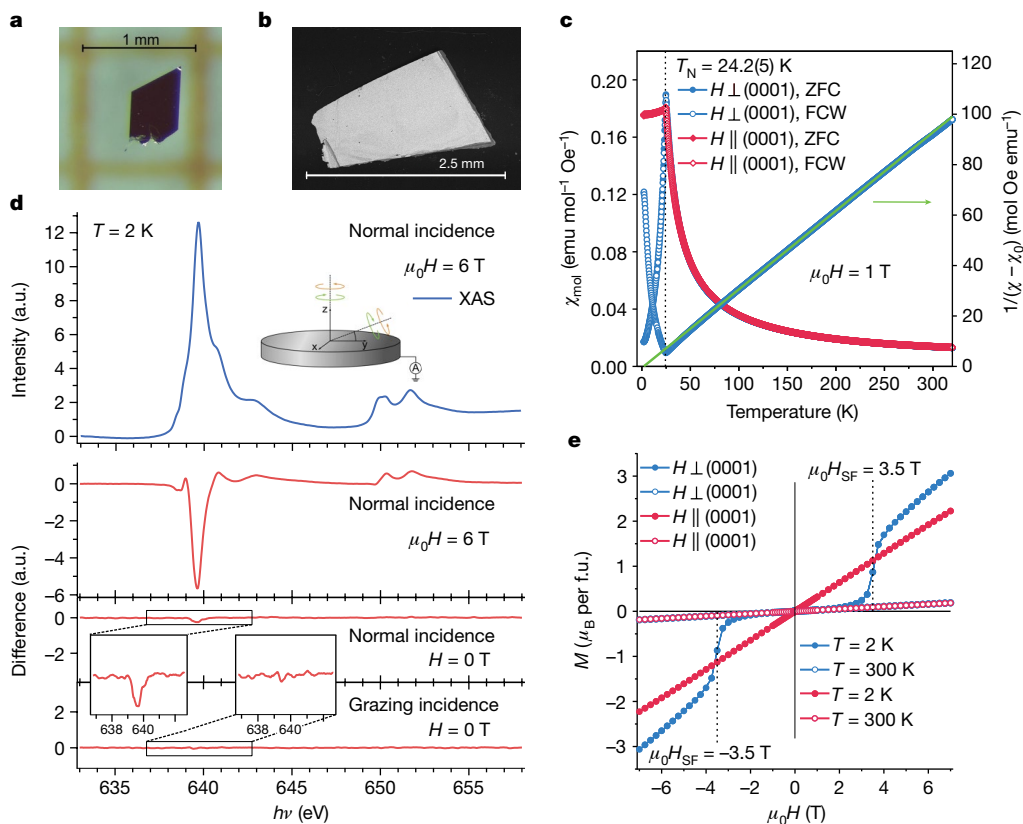
Fig. 2 | MnBi₂Te₄ single crystals and their magnetic properties. a, b, MnBi₂Te₄ single crystals: D sample (**a**, optical microscope image) and B sample (**b**, scanning electron microscope image). **c,** Magnetic susceptibility (left axis) of phase-pure MnBi₂Te₄ as a function of temperature measured in an external magnetic field of $\mu_0 H = 1$ T in zero-field-cooled (ZFC) and field-cooled-warming (FCW) conditions, alongside the temperature-dependent reciprocal susceptibility (right axis) for $H \perp (0001)$. The green line is a modified Curie–Weiss fit to the high-temperature data ($\chi_0 = 0.0028(3)$ e.m.u. mol⁻¹Oe⁻¹, 1 oersted (Oe) = 1,000/4π A m⁻¹, 1 electromagnetic unit (e.m.u.) = $4\pi \times 10^{-6}$ m³ mol⁻¹; details in text). **d,** XMCD measurements for MnBi₂Te₄ at the Mn L$_{2,3}$ edge. Inset, A sketch of the experiment. The external magnetic field is applied along the direction of light incidence. Top, The sum (X-ray absorption spectroscopy signal) and middle, the difference (XMCD signal) between the right (R) and left (L) X-ray absorption intensities I_R and I_L measured with right and left circularly polarized light in normal incidence at $\mu_0 H = 6$ T. Bottom, The XMCD signal in remanence — that is, at $H = 0$ T — for normal and grazing light incidence, measured after switching off an external field of $\mu_0 H = 6$ T along the respective directions. Insets show a magnification of the L$_3$ dichroism in remanence. **e,** Field-dependent magnetization curves for the two directions, measured at 2 K (blue) and 300 K (red). f.u., formula unit; H$_{SF}$, spin-flop magnetic field.

Monte Carlo simulations and results of the resistivity measurements (Extended Data Fig. 3a). Below T_N, a strongly anisotropic magnetic susceptibility χ is observed, which decreases more steeply for the magnetic field $H \perp (0001)$. No splitting between zero-field-cooled and field-cooled-warming curves was found. The paramagnetic regime above T_N was fitted with a modified Curie–Weiss law, $\chi(T) = \chi_0 + C/(T - \Theta_{CW})$, in the 100 K to 250 K range. Here, χ_0 is the temperature-independent magnetic susceptibility of both diamagnetic closed electron shells and a Pauli paramagnetic contribution resulting from some degree of metallicity in this material (see below). $C/(T - \Theta_{CW})$ accounts for a temperature-dependent Curie–Weiss susceptibility of the Mn local magnetic moments. The fitted effective paramagnetic moment of $5.0(2)\mu_B$ is in rough agreement with the high-spin configuration of Mn²⁺ ($S = 5/2$), and a small and positive value of the Curie–Weiss temperature ($\Theta_{CW} = 3(3)$ K) strongly depends on the fitted χ_0 contribution. The $M(H)$ curve acquired below T_N for $H \perp (0001)$ shows an indicative spin-flop transition at $\mu_0 H_{SF} \approx 3.5$ T (Fig. 2e), which is in line with an out-of-plane easy axis of the staggered magnetization.

We further performed X-ray magnetic circular dichroism (XMCD) experiments at the Mn L$_{2,3}$ absorption edge (D samples; Fig. 2d). The data were acquired in total electron yield mode with a probing depth of typically only a few nanometres. The XMCD signal obtained at an external field of 6 T and in normal light incidence verifies the magnetic polarization of the Mn ions. After removing the external field ($H = 0$) the signal collapses, as expected for an AFM ordering. However, a small residual signal is observed in remanence, indicating a finite net out-of-plane polarization within the probed volume of the sample. This residual signal appears to be inconsistent with an AFM intralayer coupling where the orientation of the moments within a Mn layer alternates on the atomic scale. However, for ferromagnetic intralayer coupling, the first septuple layer, which is preferentially probed in the total electron yield mode, is expected to be composed of mesoscopic domains with the magnetization pointing in or out of the surface plane. We attribute the residual XMCD signal in remanence to a preferential sampling of one domain type with the micrometre-sized synchrotron beam spot. This supports our first-principles calculations, which predict a ferromagnetic ordering within individual septuple layers. Performing the same experiment in grazing light incidence, that is, with sensitivity to in-plane magnetization, we observe no finite polarization in remanence.

The scope of experimental evidence (Fig. 2) enables us to identify MnBi₂Te₄ as an interlayer antiferromagnet, in which ferromagnetic Mn layers are coupled antiparallel to each other and the easy axis of staggered magnetization is perpendicular to the layers (Fig. 1d).

We studied the surface electronic structure of MnBi₂Te₄(0001) using angle-resolved photoemission spectroscopy (ARPES). The intensity
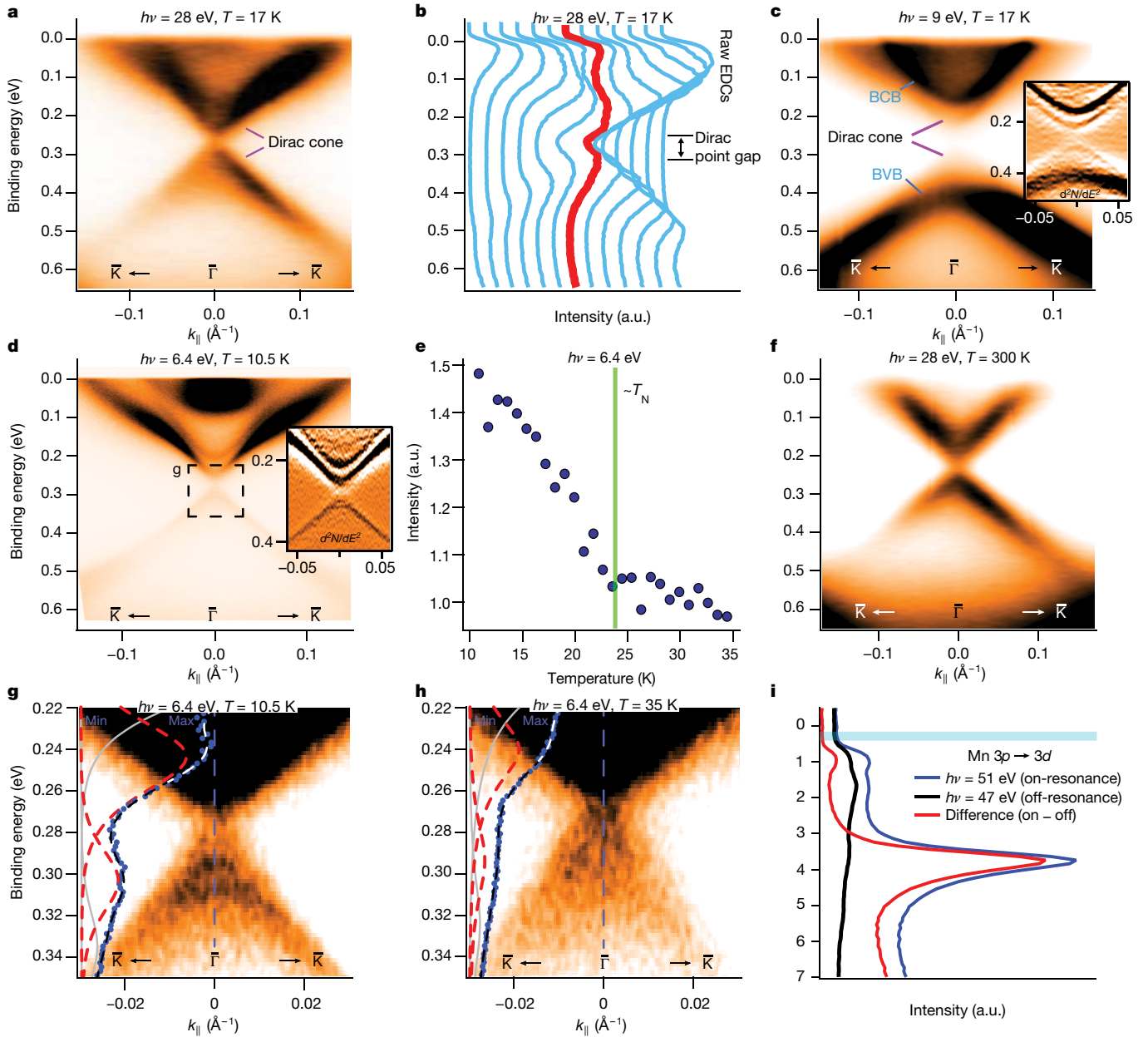
Fig. 3 | Photoemission spectroscopy insight into the surface and bulk bandstructure of MnBi₂Te₄. a, Dispersion of MnBi₂Te₄(0001) measured at 17 K with a photon energy of 28 eV. **b**, EDC representation of the data shown in **a**. The red curve marks the EDC at the $\bar{\Gamma}$-point. **c**, Dispersion of MnBi₂Te₄(0001) measured at the same temperature with a photon energy of 9 eV (which is more bulk sensitive). Inset, the corresponding second derivative ($d^2N(E)/dE^2$). BCB, bulk conduction band; BVB, bulk valence band. **d**, The same as **c**, but measured with laser photon energy of 6.4 eV, $T = 10.5$ K, and a different sample. Inset, The corresponding second derivative. The dashed rectangle around the Dirac point marks the region that is magnified in **g**. **e**, Temperature dependence of the Dirac surface state photoemission intensity calculated as a sum of the intensities of the lower and upper parts of the cone at the $\bar{\Gamma}$-point (see Methods for details). **f**, ARPES image acquired at 300 K ($h\nu = 28$ eV). **g**, **h**, Magnifications

of the Dirac point gap region of the ARPES maps taken at 10.5 K (**g**) and 35 K (**h**), with the fitted EDC spectra at the $\bar{\Gamma}$-point overlaid. The raw data, resulting fitted curves, and their decompositions with Voigt peaks are shown by blue circles, black and white lines, and grey and red lines, respectively. Red (grey) lines indicate the peaks attributed to the gapped Dirac cone state (bulk bands). The results shown in **a**–**h** were acquired on B samples. **i**, Resonant valence-band spectra of MnBi₂Te₄ taken at the Mn 3p–3d absorption edge (D samples). On- and off-resonance spectra were obtained at $h\nu = 51$ eV and $h\nu = 47$ eV, respectively. The difference between these spectra approximately reflects the density of the Mn 3d states, showing a main peak near 3.8 eV and an additional feature near 1 eV. The energy range of the bulk energy gap is marked by the horizontal cyan region.

map measured near the Brillouin zone centre at a temperature of 17 K is shown in Fig. 3a ($h\nu = 28$ eV, where h is the Planck constant and ν is the photon frequency; B sample). Two almost linearly dispersing bands form a Dirac-cone-like structure with strongly reduced intensity at the crossing point. The energy distribution curves (EDCs) reveal an energy gap of about 70 meV at the $\bar{\Gamma}$-point that separates the upper and lower parts of the cone (Fig. 3b). A similar result was obtained for the D

samples (Extended Data Fig. 4). These results agree with those of the MnBi₂Te₄(0001) surface bandstructure calculations (see Fig. 1e).

Next, we performed extensive ARPES measurements with different photon energies. At $h\nu = 9$ eV (Fig. 3c), the features that are not seen at $h\nu = 28$ eV show a pronounced spectral weight: namely, the intense electron- and hole-like bands coming to the $\bar{\Gamma}$-point at binding energies of about 0.17 eV and 0.4 eV, respectively. A comparison with the
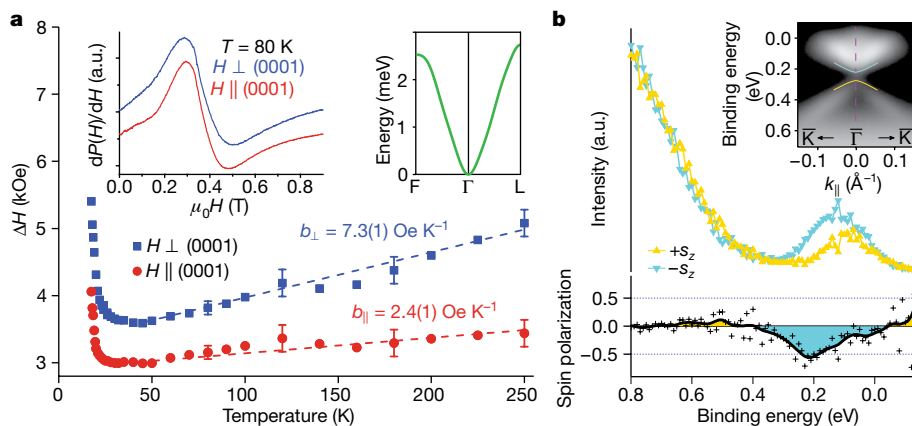
Fig. 4 | Spin characterization of bulk and surface electronic structure of MnBi$_2$Te$_4$. a, Temperature dependence of the width ΔH of the ESR signal for two directions of the magnetic field. Dashed lines are linear fits to the $\Delta H(T)$ dependence, yielding the Korringa slopes $b_{\perp,\parallel} = d[\Delta H(T)]/dT$. The error bars are derived from the fitting procedure of ESR line shapes. The larger error bars above approximately 100 K are due to the occurrence of a parasitic signal in the ESR spectrum overlapping with the main line. Left inset, Typical ESR spectra (the field derivative of the microwave absorption $dP(H)/dH$) of Mn^{2+} in MnBi$_2$Te$_4$ at $\nu = 9.6$ GHz. The measurements were done on D samples. See Methods for more information about ESR measurements of MnBi$_2$Te$_4$.

Right inset, Magnon spectrum calculated ab initio for bulk MnBi$_2$Te$_4$ in the paramagnetic state (paramagnons). **b**, Room-temperature spin-resolved ARPES spectra measured at the $\bar{\Gamma}$-point with respect to the out-of-plane spin quantization axis. The out-of-plane spin polarization is presented below the corresponding spin-up and spin-down spectra (cross symbols). Inset, Spin-integrated ARPES spectrum taken along the $\bar{K}$–$\bar{\Gamma}$–$\bar{K}$ direction. Yellow and cyan curves show the location of the gapped Dirac cone. The data were obtained for B samples at a photon energy of 6 eV. See Extended Data Fig. 10 for more spin-resolved ARPES data.

theoretically calculated bulk-projected bandstructure enables us to identify these bands as the bulk conduction and valence bands, respectively. The analysis of the $\bar{\Gamma}$-point EDC shows that both valence and conduction bands can be fitted with two peaks (Extended Data Fig. 5), in agreement with the result of our calculations, showing two bulk bands with a weak k_z dispersion both below and above the Fermi level (Fig. 1e). On the basis of the photoemission measurements, we estimate the bulk bandgap to be close to 200 meV, again in agreement with the calculated values. The second-derivative data in the inset to Fig. 3c provide further insight: along with the bulk bands the gapped Dirac cone is also seen. We note that the Fermi level cuts the conduction band, indicating the n-doped character of the samples, which is consistent with the results of the Hall measurements (see Extended Data Fig. 3b). If we artificially drive MnBi$_2$Te$_4$ into a topologically trivial phase by decreasing the SOC strength in a calculation, a strong discrepancy arises between the theory and experiment. Namely, in the trivial phase there are no surface states in the fundamental bulk bandgap (Extended Data Fig. 6). By contrast, the ARPES data acquired at different photon energies (Extended Data Fig. 7) unambiguously confirm the gapped Dirac cone to be a surface state, in agreement with the calculated (0001) surface bandstructure of the MnBi$_2$Te$_4$ AFM topological insulator (Fig. 1e).

Thus, by virtue of the good agreement between the theory and experiment, we conclude that the fundamental bandgap of MnBi$_2$Te$_4$ is inverted. Our data also confirm the trigonal structure (space group $R\bar{3}m$) and interlayer AFM order, whereby the S-symmetry is also confirmed. These results confirm the $\mathbb{Z}_2 = 1$ three-dimensional AFM topological insulator state of MnBi$_2$Te$_4$ below its Néel temperature.

The ARPES measurements above T_N were performed next. We note that increasing the temperature does not lead to the Dirac point gap closing at MnBi$_2$Te$_4$(0001); see Fig. 3f. Nevertheless, we observe a temperature dependence of a linear dichroism in the Dirac cone intensity that indicates that the AFM order influences the TSS (see Extended Data Fig. 8). Moreover, directly below T_N, the intensity of the Dirac cone starts to grow abruptly when the temperature decreases (Fig. 3e and Extended Data Fig. 9; laser ARPES with $h\nu = 6.4$ eV), signalling the paramagnet–antiferromagnet transition and showing a clear response of the surface electronic structure to the AFM ordering. In Fig. 3d, the

photoemission intensity map acquired at $T = 10.5$ K is shown. A closer look at these data around the Dirac point gap (Fig. 3g) and their comparison to the analogous spectrum taken at 35 K (Fig. 3h), reveals that substantial changes occur across the Néel temperature. In particular, the shape of the $\bar{\Gamma}$-point EDC is modified: a pronounced intensity dip owing to the Dirac point gap at around 0.28 eV seen at 10.5 K (Fig. 3g) is absent at 35 K (Fig. 3h). Nevertheless, the Dirac point gap is present in Fig. 3h, as the EDC fit was only possible using two peaks, corresponding to the Dirac point gap edges. Thus, although the paramagnet–antiferromagnet transition does not lead to closing of the Dirac point gap, the results in Fig. 3e,g,h reveal clearly the strong sensitivity of the TSS to the AFM ordering.

The presence of a Dirac point gap in the paramagnetic phase has been previously reported for the surface states of magnetically doped topological insulators[13–15]. In the case of the Bi$_{2-x}$Mn$_x$Se$_3$(0001) surface, resonant scattering processes owing to impurity states in the fundamental bandgap were suggested as a possible reason[15]. To check whether similar effects take place in our MnBi$_2$Te$_4$ samples, we performed resonant photoemission measurements at the Mn 3p–3d edge. The results, shown in Fig. 3i, reveal no resonant features and hence no Mn 3d states around the Dirac point gap, whereupon we discard such a mechanism for the Dirac point gap opening in MnBi$_2$Te$_4$.

To gain a deeper insight into the electronic properties of MnBi$_2$Te$_4$ both below and above T_N, we performed electron spin resonance (ESR) measurements (Fig. 4a; D samples). In MnBi$_2$Te$_4$, the ESR linewidth $\Delta H(T)$ shows surprising anisotropic behaviour above approximately 50 K. Namely, the so-called Korringa slope $b = d[\Delta H(T)]/dT$ of the linear $\Delta H(T)$ dependence for $H \perp (0001)$ is three times larger than that for $H \parallel (0001)$ (Fig. 4a), suggesting spatially anisotropic fluctuations of the local magnetic moments owing to their coupling to conduction electrons[16,17]. In MnBi$_2$Te$_4$, $b_\perp \gg b_\parallel$, which indicates a relatively short transversal relaxation time τ_2 of the local magnetic moments for the out-of-plane static field geometry and, thus, fast fluctuations of the Mn spins in the (0001) plane. By contrast, in the case of the in-plane field geometry, where the τ_2 relaxation time characterizes Mn spin fluctuations perpendicular to the (0001) plane, the fluctuations appear to be considerably slower, as reflected in the smaller value of $b_\parallel$. Consequently, on a timescale of the photoexcitation process in ARPES (about 10^{-15} s), which is much shorter

than the Mn spin relaxation time (about 10^{-10} s), the probability of finding a Mn spin oriented perpendicularly to (0001) may be larger than for other directions, which could effectively generate an instantaneous out-of-plane field acting on the TSS electrons even in the absence of long-range order. Indeed, our room-temperature (300 K) spin-resolved ARPES measurements reveal the out-of-plane spin components both at the $\bar{\Gamma}$-point (Fig. 4b) and at finite $k_{\parallel}$ (see Extended Data Fig. 10). Moreover, the calculated paramagnons indicate the presence of ferromagnetic correlations within individual septuple-layer blocks above T_N (Fig. 4a, right inset). Herewith, the ferromagnetically correlated moments tend to point perpendicular to the (0001) plane, which is consistent with the spin-ARPES observations, revealing out-of-plane spin polarization near the Fermi level. We thus conclude that the instantaneous out-of-plane spin polarization observed in our experiments could be responsible for the persistence of the Dirac point gap observed by ARPES in the paramagnetic state of $MnBi_2Te_4$.

Our experimental and theoretical results establish $MnBi_2Te_4$ as an AFM topological insulator. Although in our experiment $MnBi_2Te_4$ is n doped (which is typical for Bi-based bulk topological insulator crystals), it is this n doping that enables the measurement of both the TSS and the bulk energy gap with ARPES, which probes only the occupied states. A common strategy in synthesizing truly insulating topological insulator crystals is Sb-doping of the Bi sublattice of tetradymite-like compounds[2,18], which is expected to work for $MnBi_2Te_4$ as well. Note that such a tuning of composition is supposed not to affect its interlayer AFM ordering[19]. On the other hand, recent progress in the growth of topological insulator films by molecular beam epitaxy[20] gives rise to the prospect that nearly-charge-neutral $MnBi_2Te_4$ can be fabricated.

An AFM topological insulator with the type of antiferromagnetic order established here for $MnBi_2Te_4$ represents an ideal platform for observing the half-integer quantum Hall effect[6] ($\sigma_{xy} = e^2/(2h)$; where σ_{xy} and e are the Hall conductivity and electron charge, respectively), which may facilitate experimental confirmation of so-called $\theta = \pi$ quantized magnetoelectric coupling. A material showing this effect is known as an axion insulator, which until now has been sought for in magnetically doped sandwich-like topological insulator heterostructures[21,22]. Unfortunately, these have been found to show superparamagnetic behaviour[4,23] that is not seen in $MnBi_2Te_4$, which makes it a promising intrinsic axion insulator candidate. Also, the ferromagnetic septuple-layer blocks of $MnBi_2Te_4$ can be used for the fabrication of topologically nontrivial heterostructures[24,25], which are promising for realizing the quantum anomalous Hall effect[2]. Beyond topotronics, another direction of further studies of $MnBi_2Te_4$ and related materials[19,26–29] lies within the rapidly growing field of van der Waals magnets[30,31]. Strongly thickness-dependent properties, expected for van der Waals compounds in the two-dimensional limit, as well as the magnetic degrees of freedom and strong SOC of $MnBi_2Te_4$ make it an interesting candidate with which to combine the emerging fields of antiferromagnetic spintronics[32,33] and layered van der Waals materials[30,31].

We have become aware of recent theoretical[34,35] and experimental[36–42] studies on $MnBi_2Te_4$ that confirm our results. In particular, the intrinsic axion insulator state has recently been realized in AFM (that is, below the Néel temperature) $MnBi_2Te_4$ thin flakes exfoliated from a bulk single crystal[41], providing an additional proof of the AFM topological insulator state in $MnBi_2Te_4$ below T_N. Additionally, the quantized Hall effect under external magnetic field has been achieved in such flakes[40–42]. Although the observation of this effect requires the ferromagnetic state of $MnBi_2Te_4$, it could not be observed if $MnBi_2Te_4$ were topologically trivial[43].

Online content

Any methods, additional references, Nature Research reporting summaries, source data, extended data, supplementary information, acknowledgements, peer review information; details of author contributions

1. Tokura, Y., Yasuda, K. & Tsukazaki, A. Magnetic topological insulators. *Nat. Rev. Phys.* **1**, 126–143 (2019).
2. Chang, C.-Z. et al. Experimental observation of the quantum anomalous Hall effect in a magnetic topological insulator. *Science* **340**, 167–170 (2013).
3. He, Q. L. et al. Chiral Majorana fermion modes in a quantum anomalous Hall insulator-superconductor structure. *Science* **357**, 294–299 (2017).
4. Lachman, E. O. et al. Visualization of superparamagnetic dynamics in magnetic topological insulators. *Sci. Adv.* **1**, e1500740 (2015).
5. Lee, I. et al. Imaging Dirac-mass disorder from magnetic dopant atoms in the ferromagnetic topological insulator $Cr_x(Bi_{0.1}Sb_{0.9})_{2-x}Te_3$. *Proc. Natl Acad. Sci. USA* **112**, 1316–1321 (2015).
6. Mong, R. S. K., Essin, A. M. & Moore, J. E. Antiferromagnetic topological insulators. *Phys. Rev. B* **81**, 245209 (2010).
7. Qi, X.-L., Hughes, T. L. & Zhang, S.-C. Topological field theory of time-reversal invariant insulators. *Phys. Rev. B* **78**, 195424 (2008).
8. Essin, A. M., Moore, J. E. & Vanderbilt, D. Magnetoelectric polarizability and axion electrodynamics in crystalline insulators. *Phys. Rev. Lett.* **102**, 146805 (2009).
9. Li, R., Wang, J., Qi, X.-L. & Zhang, S.-C. Dynamical axion field in topological magnetic insulators. *Nat. Phys.* **6**, 284–288 (2010).
10. Wang, J., Lian, B. & Zhang, S.-C. Dynamical axion field in a magnetic topological insulator superlattice. *Phys. Rev. B* **93**, 045115 (2016).
11. Lee, D. S. et al. Crystal structure, properties and nanostructuring of a new layered chalcogenide semiconductor, Bi_2MnTe_4. *CrystEngComm* **15**, 5532–5538 (2013).
12. Hasan, M. Z. & Kane, C. L. Topological insulators. *Rev. Mod. Phys.* **82**, 3045–3067 (2010).
13. Chen, Y. L. et al. Massive Dirac fermion on the surface of a magnetically doped topological insulator. *Science* **329**, 659–662 (2010).
14. Xu, S.-Y. et al. Hedgehog spin texture and Berry's phase tuning in a magnetic topological insulator. *Nat. Phys.* **8**, 616–622 (2012).
15. Sánchez-Barriga, J. et al. Nonmagnetic band gap at the Dirac point of the magnetic topological insulator $(Bi_{1-x}Mn_x)_2Se_3$. *Nat. Commun.* **7**, 10559 (2016).
16. Vaknin, D., Davidov, D., Zevin, V. & Selig, H. Anisotropy and two-dimensional effects in the ESR properties of OsF_6-graphite intercalation compounds. *Phys. Rev. B* **35**, 6423–6431 (1987).
17. Vithayathil, J. P., MacLaughlin, D. E., Koster, E., Williams, D. L. & Bucher, E. Spin fluctuations and anisotropic nuclear relaxation in single-crystal UPt_3. *Phys. Rev. B* **44**, 4705–4708 (1991).
18. Zhang, J. et al. Band structure engineering in $(Bi_{1-x}Sb_x)_2Te_3$ ternary topological insulators. *Nat. Commun.* **2**, 574 (2011).
19. Eremeev, S. V., Otrokov, M. M. & Chulkov, E. V. Competing rhombohedral and monoclinic crystal structures in $MnPn_2Ch_4$ compounds: an ab-initio study. *J. Alloys Compd.* **709**, 172–178 (2017).
20. Wu, L. et al. Quantized Faraday and Kerr rotation and axion electrodynamics of a 3D topological insulator. *Science* **354**, 1124–1127 (2016).
21. Mogi, M. et al. A magnetic heterostructure of topological insulators as a candidate for an axion insulator. *Nat. Mater.* **16**, 516–521 (2017).
22. Xiao, D. et al. Realization of the axion insulator state in quantum anomalous Hall sandwich heterostructures. *Phys. Rev. Lett.* **120**, 056801 (2018).
23. Krieger, J. A. et al. Spectroscopic perspective on the interplay between electronic and magnetic properties of magnetically doped topological insulators. *Phys. Rev. B* **96**, 184402 (2017).
24. Otrokov, M. M. et al. Magnetic extension as an efficient method for realizing the quantum anomalous Hall state in topological insulators. *JETP Lett.* **105**, 297–302 (2017).
25. Otrokov, M. M. et al. Highly-ordered wide bandgap materials for quantized anomalous Hall and magnetoelectric effects. *2D Mater.* **4**, 025082 (2017).
26. Hirahara, T. et al. Large-gap magnetic topological heterostructure formed by subsurface incorporation of a ferromagnetic layer. *Nano Lett.* **17**, 3493–3500 (2017).
27. Hagmann, J. A. et al. Molecular beam epitaxy growth and structure of self-assembled Bi_2Se_3/Bi_2MnSe_4 multilayer heterostructures. *New J. Phys.* **19**, 085002 (2017).
28. Rienks, E. D. L. et al. Large magnetic gap at the Dirac point in a Mn-induced Bi_2Te_3 heterostructure. Preprint at https://arxiv.org/abs/1810.06238 (2018).
29. Eremeev, S. V., Otrokov, M. M. & Chulkov, E. V. New universal type of interface in the magnetic insulator/topological insulator heterostructures. *Nano Lett.* **18**, 6521–6529 (2018).
30. Gong, C. et al. Discovery of intrinsic ferromagnetism in two-dimensional van der Waals crystals. *Nature* **546**, 265–269 (2017).
31. Huang, B. et al. Layer-dependent ferromagnetism in a van der Waals crystal down to the monolayer limit. *Nature* **546**, 270–273 (2017).
32. Baltz, V. et al. Antiferromagnetic spintronics. *Rev. Mod. Phys.* **90**, 015005 (2018).
33. Šmejkal, L., Mokrousov, Y., Yan, B. & MacDonald, A. H. Topological antiferromagnetic spintronics. *Nat. Phys.* **14**, 242–251 (2018).
34. Zhang, D. et al. Topological axion states in magnetic insulator $MnBi_2Te_4$ with the quantized magnetoelectric effect. *Phys. Rev. Lett.* **122**, 206401 (2019).
35. Li, J. et al. Intrinsic magnetic topological insulators in van der Waals layered $MnBi_2Te_4$-family materials. *Sci. Adv.* **5**, eaaw5685 (2019).
36. Gong, Y. et al. Experimental realization of an intrinsic magnetic topological insulator. *Chin. Phys. Lett.* **36**, 076801 (2019).
37. Lee, S. H. et al. Spin scattering and noncollinear spin structure-induced intrinsic anomalous Hall effect in antiferromagnetic topological insulator $MnBi_2Te_4$. *Phys. Rev. Res.* **1**, 012011(R) (2019).
38. Yan, J.-Q. et al. Crystal growth and magnetic structure of $MnBi_2Te_4$. *Phys. Rev. Mater.* **3**, 064202 (2019).
39. Chen, B. et al. Intrinsic magnetic topological insulator phases in the Sb doped $MnBi_2Te_4$ bulks and thin flakes. *Nat. Commun.* **10**, 4469 (2019).

Article

40. Deng, Y. et al. Magnetic-field-induced quantized anomalous Hall effect in intrinsic magnetic topological insulator $MnBi_2Te_4$. Preprint at https://arxiv.org/abs/1904.11468 (2019).

41. Liu, C. et al. Quantum phase transition from axion insulator to Chern insulator in $MnBi_2Te_4$. Preprint at https://arxiv.org/abs/1905.00715 (2019).

42. Ge, J. et al. High-Chern-number and high-temperature quantum Hall effect without Landau levels. Preprint at https://arxiv.org/abs/1907.09947 (2019).

43. Otrokov, M. M. et al. Unique thickness-dependent properties of the van der Waals interlayer antiferromagnet $MnBi_2Te_4$ films. *Phys. Rev. Lett.* **122**, 107202 (2019).

[1]Centro de Física de Materiales (CFM-MPC), Centro Mixto CSIC-UPV/EHU, San Sebastián, Spain. [2]IKERBASQUE, Basque Foundation for Science, Bilbao, Spain. [3]Donostia International Physics Center (DIPC), San Sebastián, Spain. [4]Saint Petersburg State University, Saint Petersburg, Russia. [5]Experimentelle Physik VII, Universität Würzburg, Würzburg, Germany. [6]Faculty of Chemistry and Food Chemistry, Technische Universität Dresden, Dresden, Germany. [7]Institute of Physics, Azerbaijan National Academy of Sciences, Baku, Azerbaijan. [8]Azerbaijan State Oil and Industry University, Baku, Azerbaijan. [9]Institute for Solid State Research, Leibniz IFW Dresden, Dresden, Germany. [10]Departamento de Física de Materiales UPV/EHU, San Sebastián, Spain. [11]Institut für Theoretische Physik, Johannes Kepler Universität, Linz, Austria. [12]Tomsk State University, Tomsk, Russia. [13]Institute of Strength Physics and Materials Science, Russian Academy of Sciences, Tomsk, Russia. [14]Elektronenspeicherring BESSY II, Helmholtz-Zentrum Berlin für Materialien und Energie, Berlin, Germany. [15]Institute of Catalysis and Inorganic Chemistry, Azerbaijan National Academy of Science, Baku, Azerbaijan. [16]Institute of Solid State Physics, Russian Academy of Sciences, Chernogolovka, Russia. [17]Faculty of Physics, Technische Universität Dresden, Dresden, Germany. [18]Hiroshima Synchrotron Radiation Center, Hiroshima University, Higashi-Hiroshima, Japan. [19]Department of Physical Sciences, Graduate School of Science, Hiroshima University, Higashi-Hiroshima, Japan. [20]Elettra Sincrotrone Trieste, Trieste, Italy. [21]Advanced Light Source, Lawrence Berkeley National Laboratory, Berkeley, CA, USA. [22]Max-Planck-Institut für Mikrostrukturphysik, Halle, Germany. *e-mail: mikhail.otrokov@gmail.com; evguenivladimirovich.tchoulkov@ehu.eus

Methods

Electronic structure and total-energy calculations

Electronic structure calculations were carried out using density functional theory using the projector augmented-wave method[44], implemented in the Vienna Ab initio Simulation Package (VASP)[45,46]. The exchange–correlation energy was treated using the generalized gradient approximation[47]. The Hamiltonian contained scalar relativistic corrections and the SOC was taken into account by the second variation method[48]. To describe the van der Waals interactions we made use of the DFT-D2[49] and the DFT-D3[50,51] approaches, which gave similar results. The energy cutoff for the plane-wave expansion was set to 270 eV. All structural optimizations were performed using a conjugate-gradient algorithm and a force-tolerance criterion for convergence of 0.01 eV Å^{-1}. SOC was always included when performing relaxations.

The Mn 3d states were treated employing the GGA+U approach[52] within the Dudarev scheme[53]. The $U_{eff} = U - J$ value (where U and J are the effective on-site Coulomb and exchange interaction parameters, respectively) for the Mn 3d states was chosen to be equal to 5.34 eV, as in previous work[24–26]. Using this U_{eff} we found a good agreement with the HSE06 functional[54–56] in the fundamental bandgap and binding energy of the Mn 3d states of bulk MnBi$_2$Te$_4$. Also, we find a very good agreement of the calculated bandgap for the single MnBi$_2$Te$_4$ septuple-layer block (0.32 eV)[43] with the measured one (0.35 eV)[36]. Moreover, the indirect character of the gap is correctly reproduced as well. Note that the GGA itself unsatisfactorily describes the bandgap of a single septuple-layer MnBi$_2$Te$_4$ film both in terms of the character (it yields direct gap) and size (43 meV); using GGA+U improves the description of the $p-d$ hybridization in the system. Further testing was performed to check the stability of the results against U_{eff} variation. Namely, the bulk crystal structure was fully optimized for different U_{eff} values (3 eV, 4 eV and 5.34 eV) and then the magnetic ordering was studied. It was found that the AFM ground state does not change upon such variations of U_{eff} and the crystal structure. The MnBi$_2$Te$_4$ magnetic anisotropy was found to be stable against these variations as well.

To model the interlayer AFM structure in MnBi$_2$Te$_4$, we used a rhombohedral cell with 14 atoms. These calculations were performed with a three-dimensional Brillouin zone sampled by a $9 \times 9 \times 9$ k-point grid.

The magnetic anisotropy energy, $E_a = E_{diff} + E_d$, was calculated taking into account the total energy differences of various magnetization directions, $E_{diff} = E_{in-plane} - E_{out-of-plane}$, and the energy of the classical dipole–dipole interaction, E_d. To calculate E_{diff}, the energies for three inequivalent magnetization directions (Cartesian x, y (in-plane) and z (out-of-plane)) were calculated and E_{diff} was determined to be the difference $E_{in-plane} - E_z$, where $E_{in-plane}$ is the energy of the most energetically favourable in-plane direction of the magnetization. A k-mesh of 2,197 points was chosen, and the total energies were calculated self-consistently for all considered directions. The calculations of E_{diff} were done for the interlayer AFM state in the cell containing 14 atoms (Fig. 1d). The energy convergence criterion was set to 10^{-7} eV, giving a well converged E_{diff} (up to a few tenths of a millielectronvolt) and excluding 'accidental' convergence. A cutoff radius of at least 20 μm was used to calculate E_d.

The $\mathbb{Z}_2$ invariant for the three-dimensional AFM topological insulator was calculated according to ref. [57]. When spatial inversion symmetry is present in the system, as it is in the MnBi$_2$Te$_4$ case, the following $\mathbb{Z}_2$-invariant ζ_0 can be defined:

$$(-1)^{\zeta_0} = \prod_{\mathbf{k}_{inv} \in B-TRIM, n \in occ/2} \zeta_n(\mathbf{k}_{inv})$$

where ζ_n is the parity of the nth occupied (occ) band and B-TRIM are special momenta $\mathbf{k}_{inv}$ in which each level is doubly degenerate, see ref. [57] for further details.

The MnBi$_2$Te$_4$ semi-infinite surface was simulated within a model of repeating films separated by a vacuum gap of a minimum of 10 Å. A 56-atomic-layers-thick slab was used, which corresponds to eight septuple layers. The interlayer distances were optimized for the topmost septuple-layer block of each surface. Both the structural optimizations and static electronic structure calculations were performed using a k-point grid of $11 \times 11 \times 1$ in the two-dimensional Brillouin zone.

Exchange-coupling constants calculations

For the equilibrium structures obtained with VASP, we calculated the Heisenberg exchange-coupling constants $J_{0,j}$ also from first principles, this time using the full-potential linearized augmented plane waves (FLAPW) formalism[58] as implemented in FLEUR[59]. We took the GGA+U approach[60,61] under the fully localized limit[62]. For the self-consistent FLAPW basis set in the MnBi$_2$Te$_4$ compound we chose a dense $22 \times 22 \times 22$ Monkhorst–Pack k-point sampling of the first Brillouin zone and a cutoff of 3.4 hartree (1 hartree = $2R_\infty hc$; R_∞ is the Rydberg constant). The density and potential expansions were cut at 10.4 hartree. Locally, muffin-tin-sphere radii values of 2.74 atomic units for Mn and 2.81 atomic units for Bi and Te atoms were used, and the partial wavefunctions were expanded up to cutoffs of the orbital angular momentum, $l = 8$. Mn, Bi, and Te contribute 4s3d, 5s5p and 6s6p valence electrons, respectively. We verified that these settings accurately reproduce the bandstructures obtained with VASP, both with and without SOC effects. The ferromagnetic versus AFM ordering energy differences are also in agreement.

The $J_{0,j}$ constants were extracted by Fourier inversion of the magnon energy dispersion for the MnBi$_2$Te$_4$ primitive cell[59,63,64], neglecting SOC. These dispersion energies, calculated in the force theorem approach, correspond to a constrained set of non-collinear spin configurations characterized by the magnon q vectors of a $13 \times 13 \times 13$ grid[59,65]. The reference self-consistent electron wavefunctions were obtained with a $12 \times 12 \times 12$ k-grid. These grids ensured that magnon energies converged below 0.1 meV and enabled us to add up to 150 neighbouring atoms to the Fourier analysis, ensuring accurate $J_{0,j}$ values.

Paramagnons calculations

Paramagnetic fluctuations were calculated within a first-principles approach based on the coherent potential approximation[66–69]. The disordered local moment method was used to take ensemble averages over the orientational configurations of the local moments[70]. Paramagnons are calculated considering the response of the disordered local moment paramagnetic state to the application of an external, site-dependent, magnetic field[71].

Ab-initio-based tight-binding calculations

Ab-initio-based tight-binding calculations were performed using the VASP package with the *Wannier90* interface[72,73]. The Wannier basis chosen consisted of six spinor p-type orbitals $\left|p_x^\uparrow\right\rangle, \left|p_y^\uparrow\right\rangle, \left|p_z^\uparrow\right\rangle, \left|p_x^\downarrow\right\rangle, \left|p_y^\downarrow\right\rangle, \left|p_z^\downarrow\right\rangle$ of Bi and Te. The surface electronic band structure was calculated within the semi-infinite medium Green's function approach[74,75].

Monte Carlo simulations

The Monte Carlo simulations were based on a classical Heisenberg Hamiltonian that includes the magnetic anisotropy energy E_a

$$\mathcal{H} = -\frac{1}{2}\sum_{ij} J_{i,j}\mathbf{e}_i \cdot \mathbf{e}_j + \sum_i E_a(\mathbf{e}_i^z)^2$$

where the magnetic moments at site i and j are described by unit vectors $\mathbf{e}_i$ and $\mathbf{e}_j$, respectively, and the magnetic coupling constants $J_{i,j}$ are determined by ab initio calculations as described above. The term of the magnetic anisotropy takes into account only the z component of the magnetic moment. For the simulation of the bulk system we created a cluster with periodic boundary conditions. Therein, the cluster size was varied with the primitive unit cell repeated N times in all directions with

Article

$N = 12, 14, \ldots, 20$. Varying the system size in this way enabled us to avoid finite size effects. We tentatively started the calculation at a temperature of 60 K and reduced T stepwise until 0.001 K. At each temperature step, the thermal equilibrium was reached after 40,000 Monte Carlo steps (chosen after comparing results for 20,000 to 100,000 steps for all systems). The same number of steps was then used to derive the observables after reaching thermal equilibrium. One Monte Carlo step represents the creation of a new random spin direction, which is either accepted or not depending on the energy difference and the current temperature. The critical temperature was finally obtained from the peak in the magnetic susceptibility, which represented the clearest identification criterion.

Crystal growth

Dresden samples (D samples). High-quality bulk single crystals of $MnBi_2Te_4$ were grown from the melt by slow cooling of a 1:1 mixture of the binary compounds Bi_2Te_3 and α-MnTe. The binaries were synthesized by mechanical pre-activation and annealing of stoichiometric mixtures of the elements. Crystal size and quality were controlled via different cooling rates within a narrow temperature interval at around 600 °C and varying annealing times. Further details of crystal-growth optimization are reported elsewhere[76]. Single-crystal X-ray diffraction was measured on a four-circle CCD diffractometer (Kappa APEX II, Bruker) with a graphite(002)-monochromator and a CCD-detector at $T = 296(2)$ K. Mo-Kα radiation ($\lambda = 71.073$ pm) was used. A numerical absorption correction based on an optimized crystal description[77] was applied, and the initial structure solution was performed in the JANA2006[78] software. The structure was refined in the SHELXL program against the experimentally observed squared structure factors F_o^2 (ref. [79,80]). The crystal structure has been deposited in the joint Cambridge Crystallographic Data Centre/FIZ Karlsruhe under depository number CSD-1867581. The structure refinement yields some degree of statistical cation disorder in the Mn and Bi positions in contrast to an earlier reported ordered model[11]. However, Mn/Bi antisite defects in two fully occupied cation positions do not lead to a superstructure ordering or change of translational symmetry. Energy dispersive X-ray spectra (EDS) were collected using a Silicon Drift X-MaxN (Oxford Instruments) detector at an acceleration voltage of 20 kV and an accumulation time of 100 s. The analysis was performed using the P/B-ZAF standardless method (where Z = atomic number correction factor, A = absorption correction factor, F = fluorescence factor and P/B = peak-to-background model). Energy dispersive X-ray spectra reproducibly yielded a stoichiometric composition, ruling out the possibility of large compositional variations in our samples.

Baku samples (B samples). The bulk ingot of the Baku sample was grown from the melt with a non-stoichiometric composition using the vertical Bridgman method. The pre-synthesized polycrystalline sample was evacuated in a conical-bottom quartz ampoule sealed under vacuum better than 10^{-4} Pa. In order to avoid any reaction during the melting process between the Mn content of the sample and the silica container, the inside wall of the ampoule was coated with graphite by thermal decomposition of acetone in an oxygen-poor environment. The ampoule was held in the 'hot' zone (about 680 °C) of a two-zone tube furnace of the $MnBi_2Te_4$ Bridgman crystal-growth system for 8 h to achieve a complete homogenization of the melts. Then, it moved from the upper (hot) zone to the bottom (cold) zone with a required rate of 0.7 mm h^{-1}. Consequently, we obtained a bulk ingot with average dimensions of 3 cm in length and 0.8 cm in diameter. Further details are reported elsewhere[81]. The as-grown ingot was checked by X-ray diffraction measurements and was found to consist of several single crystalline blocks. With the aid of X-ray diffraction data, high-quality single crystalline pieces were isolated from different parts of the as-grown ingot for further measurements.

Magnetic measurements

The magnetic measurements as a function of temperature and magnetic field were performed on a stack of single crystals of $MnBi_2Te_4$ (D samples) using a SQUID (superconducting quantum interference device) VSM (vibrating-sample magnetometer) (Quantum Design). The temperature-dependent magnetization measurements were acquired in external magnetic fields of 0.02 T and 1 T for both zero-field-cooled and field-cooled-warming conditions. A thorough background subtraction was performed for all curves.

Part of the magnetic measurements were carried out at the Center for Diagnostics of Materials for Medicine, Pharmacology and Nanoelectronics of the SPbU Science Park using a SQUID magnetometer with a helium cryostat (Quantum Design). The measurements were carried out in a pull mode in terms of temperature and magnetic field. The applied magnetic field was perpendicular to the (0001) sample surface.

Resistivity measurements

Resistivity measurements were done with a standard four-probe ac technique using a low-frequency ($f \approx 20$ Hz) lock-in amplifier. Contacts were attached with conducting graphite paste. The measurements were carried out in a temperature-variable cryostat at different values of magnetic field up to 8 T, generated by a superconducting solenoid and directed along the normal to the (0001) sample surface.

Temperature- and field-dependent resistivity measurements were performed on B samples (Extended Data Fig. 3a). The metallic-like behaviour characteristic of the presence of free carriers is observed at $H = 0$ as the resistivity ρ increases with rising temperature. This is consistent with the results of the Hall-effect measurements yielding the n-type conductivity of these samples (Extended Data Fig. 3b). A well defined kink at 25.4 K indicates a magnetic transition in agreement with the magnetization studies and Monte Carlo simulations. In a series of measurements under an external field $H \perp$ (0001), the kink shifts to lower temperatures as the field increases from 1 T to 3 T. Above the critical field (around 3 T to 4 T), the $\rho(T)$ slope is much steeper below T_N, which could be related to the observed spin-flop in the $M(H)$ curve (Fig. 2e).

ESR measurements

ESR experiments were performed with a commercial X-band ESR-spectrometer (EMX, Bruker) operating at a microwave frequency of 9.6 GHz and providing magnetic fields up to 0.9 T. It is equipped with a He gas flow cryostat (Oxford Instruments) and a goniometer allowing temperature- and angular-dependent measurements between 4 K and 300 K.

The temperature dependence of the resonance field H_{res} of the ESR signal of Mn^{2+} ions in $MnBi_2Te_4$ is measured for the out-of-plane $H \perp$ (0001) and in-plane $H \parallel$ (0001) orientations of the static magnetic field H. At high temperatures H_{res} is almost isotropic within the error bars of ±80 Oe, and the corresponding spectroscopic g-factor is very close to the spin-only value $g_s = 2$, as expected for the Mn^{2+} ($3d^5$; spin angular momentum $S = 5/2$; orbital angular momentum $L = 0$) ion[82]. However, below $T \approx 50$ K, H_{res} becomes anisotropic and, in particular, the resonance line rapidly shifts to smaller fields for the out-of-plane geometry—indicating the onset of quasi-static short-range magnetic correlations in $MnBi_2Te_4$ well above the AFM phase transition at T_N. By further lowering the temperature, the linewidth experiences critical broadening due to the slowing down of the spin fluctuations in the vicinity[83] of T_N (Fig. 4a). Finally, upon entering the AFM-ordered state the intensity of the ESR signal rapidly decreases, owing to the shifting of the spectral weight to the AFM collective resonance modes, which typically occur at much higher frequencies than the paramagnetic resonance[84], and thus out of the frequency range of our ESR setup. Observation of quasi-static short-range magnetic correlations in the ESR experiment is consistent with the strong spin fluctuation-driven

spin scattering above T_N found in a previous magneto-transport study[37] of MnBi$_2$Te$_4$.

ARPES measurements

The ARPES experiments were carried out at the BaDELPh beamline[85] of the Elettra synchrotron in Trieste (Italy) and BL-1 of the Hiroshima synchrotron radiation centre (Japan) using p polarization of the synchrotron radiation and laser[86,87]. The photoemission spectra were collected on freshly cleaved surfaces. The base pressure during the experiments was better than 1×10^{-10} mbar. Some of the ARPES experiments were also carried out at the resource centre Physical Methods of Surface Investigation (PMSI) at the research park of Saint Petersburg State University.

Additional hv-dependent experiments on D samples (data shown in Extended Data Fig. 7) were performed at the MAESTRO endstation of the Advanced Light Source facility.

Dichroic ARPES measurements

The linear dichroism ARPES measurements on D samples (Extended Data Fig. 8) were performed at the MAESTRO endstation of the Advanced Light Source facility. This measurement enabled us to explore the influence of the AFM state on the wavefunction of the TSS. With p-polarized light incident in the x–z plane the linear dichroism (LD) in the photoelectron intensity (I) can be defined as[88–91]:

$$LD(k_x, k_y, E) = I(k_x, k_y, E) - I(-k_x, k_y, E)$$

The linear dichroism is the intensity asymmetry relative to the y–z plane. In the present experiment the y–z plane is a crystalline mirror plane. Therefore, in the absence of a magnetization, the linear dichroism is induced by the mirror-symmetry breaking of the light electric field vector $\boldsymbol{\varepsilon} = (\varepsilon_x, 0, \varepsilon_z)$. The intensities along $\pm k_x$ can be written as $I(\pm k_x) = |T_z \pm T_x|^2$, where T_z and T_x are the photoemission matrix elements of the electric field components ε_z and ε_x between the photoelectron final state Φ_f and the initial state ψ_i at a given k_x (ref. [88]). We find LD $= 4\Re(T_z^* T_x)$, where $\Re$ denotes the real part and the asterisk indicates the complex conjugate, implying that a change of either matrix element will also change the linear dichroism. In particular, a change of the TSS wavefunction across T_N will manifest in the linear dichroism because the TSS enters the matrix elements as the initial-state wavefunction ψ_i.

This is precisely what we observe in Extended Data Fig. 8a–c: at temperatures above T_N a linear dichroism is already present, but it considerably increases below T_N. This effect is understood as the effect of the AFM order on ψ_i. In the present case, as described in the text, T_N marks the transition between the AFM state and a paramagnetic state with anisotropic fluctuations. Our linear-dichroism measurements provide strong evidence for an effect of the AFM order on the TSS wavefunction.

Our theoretical calculations provide additional insight into the origin of the linear dichroism. The crystal structure of the (0001) surface of MnBi$_2$Te$_4$ has three mirror planes along the $\overline{\Gamma}$–$\overline{M}$ directions of the two-dimensional Brillouin zone. In the nonmagnetic case, the presence of these mirror planes dictates that the out-of-plane spin components are zero for the $\overline{\Gamma}$–$\overline{M}$ directions, along which the spins are locked exclusively within the surface plane. However, for the $\overline{\Gamma}$–$\overline{K}$ directions the s_z components are allowed by symmetry and can therefore coexist with the in-plane spins. As can be seen in a previous work[24], in the case of an isostructural compound GeBi$_2$Te$_4$, ab initio calculations reveal the presence (absence) of the out-of-plane spins for the $\overline{\Gamma}$–$\overline{K}$ ($\overline{\Gamma}$–$\overline{M}$) directions. At GeBi$_2$Te$_4$(0001), the out-of-plane spin components are especially pronounced away from the fundamental bandgap energy region, where the TSS coincides with the bulk states in energy (but not in $k_\parallel$). By analogy, the appearance of the out-of-plane spin components along $\overline{\Gamma}$–$\overline{K}$ can be expected for the TSS of MnBi$_2$Te$_4$(0001). Such a spin texture is required to respect the time-reversal symmetry if the AFM exchange field inherent to the material is artificially set to zero. In this case, the

sign of s_z will change upon changing $+k_\parallel$ (right branch) to $-k_\parallel$ (left branch). When the time-reversal symmetry is broken and each MnBi$_2$Te$_4$ septuple layer is ferromagnetically ordered, the right and left branches of the TSS interact differently with the Zeeman field provided by the Mn layer of the topmost septuple-layer block (Extended Data Fig. 8d). This is similar to the so-called exchange+Rashba effect[92,93]. In such cases, a dispersion asymmetry is created—that is, $E(+k_\parallel) \neq E(-k_\parallel)$—which is indeed seen for the MnBi$_2$Te$_4$ TSS (Extended Data Fig. 8d, e), resulting in a sizeable asymmetry in the orbital composition between its right and left branches (Extended Data Fig. 8e, f). Note that such asymmetries are not found in our calculations for the $\overline{\Gamma}$–$\overline{M}$ directions because of the symmetry constraints on the presence of s_z components in the case of time-reversal-symmetry preservation. In the time-reversal symmetry breaking case, the s_z components appear along the $\overline{\Gamma}$–$\overline{M}$ directions, which also breaks the mirror symmetry at the MnBi$_2$Te$_4$(0001) surface.

Temperature-dependent laser ARPES measurements

To study the Dirac cone state response to the onset of the AFM order, we carried out the temperature-dependent high-resolution laser ARPES measurements for the MnBi$_2$Te$_4$(0001) surface. In Extended Data Fig. 9a, the raw EDC profiles at the $\overline{\Gamma}$-point at 10.5 K and 35 K are presented (as in Fig. 3g, h), clearly showing the increase of the intensities of both the upper and lower parts of the Dirac cone state below the Néel temperature. Before studying the Dirac cone intensity variation systematically, we analysed the intensity of the first two bulk conduction-band states (those shown in the Extended Data Fig. 5c). No temperature dependence of the integral intensity of these bulk states was observed (Extended Data Fig. 9b) and therefore the EDC spectra require no specific temperature-dependent normalization. Thus, the intensity temperature dependence was obtained using the raw ARPES data. The results are shown in Extended Data Fig. 9c, where the $\overline{\Gamma}$-point EDC profiles, acquired with a temperature step of around 0.9 K, are plotted versus temperature. Below about 24–25 K, the increase in intensity in the $\Delta E = [0.2$ eV, 0.3 eV$]$ energy window, containing the Dirac cone state at the $\overline{\Gamma}$-point, is clearly seen. Note that these temperature-dependent ARPES spectra were measured with the equal acquisition time and the constant laser photon flux for each temperature point in Extended Data Fig. 9c. In order to obtain a deeper insight into this intensity behaviour, we integrate it within the energy window ΔE and plot as a function of temperature in Extended Data Fig. 9d (the same data are presented in Fig. 3e of the manuscript). We see that although the Dirac cone intensity is roughly constant above $T_N \approx 24$ K, below the Néel temperature it starts to grow, and at 10 K it increases by a factor of 1.4–1.5 compared to its value at 35 K.

We note that during the ARPES measurements the spectra acquisition time is limited, which is due to a finite 'lifetime' of the clean surface of the sample even under the ultrahigh-vacuum conditions. This lifetime is comparable to the time needed to acquire several high-quality ARPES maps (such as shown in Fig. 3g, h), that are suitable for a reliable comparative EDC spectral analysis (fitting). However, within the lifetime of the clean surface of the sample, such a long acquisition time per temperature point is unreachable during the systematic temperature-dependent measurements that in our case are made with more than 50 temperature points, that is, $\Delta T \approx 0.9$ K and two sweep directions (10 K → 35 K → 10 K). Although the measured EDCs shown in Extended Data Fig. 9c are clearly meaningful, their spectral decomposition (fitting), similar to that shown in Extended Data Fig. 9a, is not unambiguous. Treated without any normalization, these raw data clearly show a strong change of intensity across the Néel temperature.

As can be seen from the EDC analysis (Extended Data Fig. 9a), the intensity increase observed is largely a result of the increase in intensity of the gapped Dirac cone peaks; the signal between those peaks (that is, within the Dirac point gap) is practically the same for 10.5 K and 35 K. Therefore, at 35 K the intensity inside the Dirac point gap increases

Article

relative to those of the Dirac cone peaks, indicative of an increase in the spectral weight inside the gap. The temperature-dependent change of the line shape around the Dirac point gap can be nicely demonstrated by the behaviour of the second derivative $(d^2N(E)/dE^2)$, which is highly sensitive to the curvature of the spectrum $N(E)$ (see Extended Data Fig. 9e). Indeed, at low temperatures we see a pronounced feature of the second derivative around the binding energy of 0.25 eV, signalling the presence of the Dirac point gap, although above the Néel temperature this feature is substantially weaker. These changes demonstrate the gapped state mitigation across the antiferromagnet–paramagnet transition.

Spin-resolved ARPES measurements

Spin-resolved ARPES measurements were performed at the RGBL-2 end-station of BESSY II in Berlin (Germany) using a hemispherical analyser (Scienta R4000) and a photon energy of 6 eV. The photon beam was generated using the fourth harmonic of a custom-made femtosecond-laser system coupled to an ultrafast amplifier operating at a repetition rate of 100 kHz. The spin-resolved spectra were acquired with a three-dimensional Mott-type spin detector operated at 26 kV. We used the vertical linearly polarized light incident on the sample under an angle of 45° with respect to the surface normal. The experimental geometry is given in ref. [94]. The energy and angular resolutions of the spin-resolved measurements were 30 meV and 1.5° (corresponding to 0.02 Å^{-1}), respectively.

Resonant photoemission measurements

Resonant photoemission data were acquired at the HR-ARPES branch of the I05 beamline at the Diamond Light Source. The measurements were conducted at a base temperature of $T = 10$ K with beam spot size and energy resolution of $A_{spot} \approx 50 \times 50$ μm^2 and $E \approx 20$ meV, respectively. The difference between on- and off-resonance spectra for the Mn $3p$–$3d$ transition corresponds directly to the density of the Mn $3d$ states. A photon energy series was conducted to determine suitable transition energies. The corresponding angle integrated spectra of on-resonance ($hv = 51$ eV) and off-resonance ($hv = 47$ eV) conditions can be seen in Fig. 3i.

XMCD measurements

Surface-sensitive XMCD measurements (total electron yield mode)[95] on D samples were performed at the HECTOR end-station of the BOREAS beamline at the ALBA synchrotron radiation facility[96]. The spot size and the resolving power of the supplied photon beam were $A_{spot} < 200 \times 200$ μm^2 and $E/\Delta E > 9,000$, respectively. Measurements were performed at the Mn $L_{2,3}$ edges at a temperature of 2 K, that is, well below $T_N \approx 24$ K.

Data availability

The data that support the findings of this study are available from the corresponding author upon reasonable request. The crystal structure is available in the joint Cambridge Crystallographic Data Centre/FIZ Karlsruhe (https://www.ccdc.cam.ac.uk/structures/) under the depository number CSD-1867581.

44. Blöchl, P. E. Projector augmented-wave method. *Phys. Rev. B* **50**, 17953–17979 (1994).
45. Kresse, G. & Furthmüller, J. Efficient iterative schemes for ab initio total-energy calculations using a plane-wave basis set. *Phys. Rev. B* **54**, 11169–11186 (1996).
46. Kresse, G. & Joubert, D. From ultrasoft pseudopotentials to the projector augmented-wave method. *Phys. Rev. B* **59**, 1758–1775 (1999).
47. Perdew, J. P., Burke, K. & Ernzerhof, M. Generalized gradient approximation made simple. *Phys. Rev. Lett.* **77**, 3865–3868 (1996).
48. Koelling, D. D. & Harmon, B. N. A technique for relativistic spin-polarised calculations. *J. Phys. C* **10**, 3107 (1977).
49. Grimme, S. Semiempirical GGA-type density functional constructed with a long-range dispersion correction. *J. Comput. Chem.* **27**, 1787–1799 (2006).
50. Grimme, S., Antony, J., Ehrlich, S. & Krieg, H. A consistent and accurate ab initio parametrization of density functional dispersion correction (DFT-D) for the 94 elements H-Pu. *J. Chem. Phys.* **132**, 154104 (2010).
51. Grimme, S., Ehrlich, S. & Goerigk, L. Effect of the damping function in dispersion corrected density functional theory. *J. Comput. Chem.* **32**, 1456–1465 (2011).
52. Anisimov, V. I., Zaanen, J. & Andersen, O. K. Band theory and Mott insulators: Hubbard *U* instead of Stoner *I*. *Phys. Rev. B* **44**, 943–954 (1991).
53. Dudarev, S. L., Botton, G. A., Savrasov, S. Y., Humphreys, C. J. & Sutton, A. P. Electron-energy-loss spectra and the structural stability of nickel oxide: An LSDA+U study. *Phys. Rev. B* **57**, 1505–1509 (1998).
54. Becke, A. D. Density-functional exchange-energy approximation with correct asymptotic behavior. *Phys. Rev. A* **38**, 3098 (1988).
55. Perdew, J. P., Ernzerhof, M. & Burke, K. Rationale for mixing exact exchange with density functional approximations. *J. Chem. Phys.* **105**, 9982–9985 (1996).
56. Heyd, J., Scuseria, G. E. & Ernzerhof, M. Hybrid functionals based on a screened Coulomb potential. *J. Chem. Phys.* **118**, 8207–8215 (2003).
57. Fang, C., Gilbert, M. J. & Bernevig, B. A. Topological insulators with commensurate antiferromagnetism. *Phys. Rev. B* **88**, 085406 (2013).
58. Wimmer, E., Krakauer, H., Weinert, M. & Freeman, A. J. Full-potential self-consistent linearized-augmented-plane-wave-method for calculating the electronic structure of molecules and surfaces: O$_2$ molecule. *Phys. Rev. B* **24**, 864–875 (1981).
59. FLEUR http://www.flapw.de, version fleur.26e (2017).
60. Anisimov, V. I., Aryasetiawan, F. & Lichtenstein, A. I. First-principles calculations of the electronic structure and spectra of strongly correlated systems: the LDA+U method. *J. Phys. Condens. Matter* **9**, 767 (1997).
61. Shick, A. B., Liechtenstein, A. I. & Pickett, W. E. Implementation of the LDA+*U* method using the full-potential linearized augmented plane-wave basis. *Phys. Rev. B* **60**, 10763–10769 (1999).
62. Anisimov, V. I., Solovyev, I. V., Korotin, M. A., Czyżyk, M. T. & Sawatzky, G. A. Density-functional theory and NiO photoemission spectra. *Phys. Rev. B* **48**, 16929–16934 (1993).
63. Sandratskii, L. M. & Bruno, P. Exchange interactions and Curie temperature in (Ga,Mn)As. *Phys. Rev. B* **66**, 134435 (2002).
64. Ležaić, M., Mavropoulos, P., Enkovaara, J., Bihlmayer, G. & Blügel, S. Thermal collapse of spin polarization in half-metallic ferromagnets. *Phys. Rev. Lett.* **97**, 026404 (2006).
65. Kurz, P., Förster, F., Nordström, L., Bihlmayer, G. & Blügel, S. Ab initio treatment of noncollinear magnets with the full-potential linearized augmented plane wave method. *Phys. Rev. B* **69**, 024415 (2004).
66. Soven, P. Coherent-potential model of substitutional disordered alloys. *Phys. Rev.* **156**, 809 (1967).
67. Gyorffy, B. L. Coherent-potential approximation for a nonoverlapping-muffin-tin-potential model of random substitutional alloys. *Phys. Rev. B* **5**, 2382 (1972).
68. Lüders, M., Ernst, A., Temmerman, W. M., Szotek, Z. & Durham, P. J. Ab initio angle-resolved photoemission in multiple-scattering formulation. *J. Phys. Condens. Matter* **13**, 8587 (2001).
69. Geilhufe, M. et al. Numerical solution of the relativistic single-site scattering problem for the Coulomb and the Mathieu potential. *J. Phys. Condens. Matter* **27**, 435202 (2015).
70. Gyorffy, B. L., Pindor, A. J., Staunton, J., Stocks, G. M. & Winter, H. A first-principles theory of ferromagnetic phase transitions in metals. *J. Phys. F* **15**, 1337 (1985).
71. Staunton, J., Gyorffy, B. L., Pindor, A. J., Stocks, G. M. & Winter, H. Electronic structure of metallic ferromagnets above the Curie temperature. *J. Phys. F* **15**, 1387 (1985).
72. Marzari, N. & Vanderbilt, D. Maximally localized generalized Wannier functions for composite energy bands. *Phys. Rev. B* **56**, 12847 (1997).
73. Mostofi, A. A. et al. wannier90: A tool for obtaining maximally-localized Wannier functions. *Comput. Phys. Commun.* **178**, 685–699 (2008).
74. Lopez Sancho, M. P., Lopez Sancho, J. M., Sancho, J. M. L. & Rubio, J. Highly convergent schemes for the calculation of bulk and surface Green functions. *J. Phys. F* **15**, 851–858 (1985).
75. Henk, J. & Schattke, W. A subroutine package for computing Green's functions of relaxed surfaces by the renormalization method. *Comput. Phys. Commun.* **77**, 69–83 (1993).
76. Zeugner, A. et al. Chemical aspects of the candidate antiferromagnetic topological insulator MnBi$_2$Te$_4$. *Chem. Mater.* **31**, 2795–2806 (2019).
77. *X-Shape, Crystal Optimization for Numerical Absorption Correction Program* Version 2.12.2, https://www.stoe.com/product/software-x-area/ (Stoe & Cie, 2009).
78. Petricek, V., Dusek, M. & Palatinus, L. *Jana2006* http://jana.fzu.cz (Institute of Physics, 2011).
79. Sheldrick, G. M. *SHELXL* Version 2014/7 https://shelx.uni-goettingen.de (Georg-August-Universität Göttingen, 2014).
80. Sheldrick, G. M. A short history of SHELX. *Acta Crystallogr. A* **64**, 112–122 (2008).
81. Aliev, Z. S. et al. Novel ternary layered manganese bismuth tellurides of the MnTe-Bi$_2$Te$_3$ system: synthesis and crystal structure. *J. Alloys Compd.* **789**, 443–450 (2019).
82. Abragam, A. & Bleaney, B. *Electron Paramagnetic Resonance of Transition Ions* (Oxford University Press, 2012).
83. Benner, H. & Boucher, J. In *Magnetic Properties of Layered Transition Metal Compounds* 323–378 (Kluwer, 1990).
84. Turov, E. A. *Physical Properties of Magnetically Ordered Crystals* (Academic Press, 1965).
85. Petaccia, L. et al. BaD ElPh: a 4-m normal-incidence monochromator beamline at Elettra. *Nucl. Instrum. Methods Phys. Res. A* **606**, 780–784 (2009).
86. Iwasawa, H. et al. Rotatable high-resolution ARPES system for tunable linear-polarization geometry. *J. Synchrotron Radiat.* **24**, 836–841 (2017).
87. Iwasawa, H. et al. Development of laser-based scanning μ-ARPES system with ultimate energy and momentum resolutions. *Ultramicroscopy* **182**, 85–91 (2017).
88. Bentmann, H. et al. Strong linear dichroism in spin-polarized photoemission from spin–orbit-coupled surface states. *Phys. Rev. Lett.* **119**, 106401 (2017).
89. Chernov, S. V. et al. Anomalous *d*-like surface resonances on Mo(110) analyzed by time-of-flight momentum microscopy. *Ultramicroscopy* **159**, 453–463 (2015).
90. Tusche, C. et al. Multi-MHz time-of-flight electronic bandstructure imaging of graphene on Ir(111). *Appl. Phys. Lett.* **108**, 261602 (2016).

91. Schönhense, G. et al. Spin-filtered time-of-flight *k*-space microscopy of Ir towards the complete photoemission experiment. *Ultramicroscopy* **183**, 19–29 (2017).
92. Krupin, O. et al. Rashba effect at magnetic metal surfaces. *Phys. Rev. B* **71**, 201403 (2005).
93. Rybkin, A. G. et al. Magneto-spin–orbit graphene: interplay between exchange and spin–orbit couplings. *Nano Lett*. **18**, 1564–1574 (2018).
94. Sánchez-Barriga, J. et al. Subpicosecond spin dynamics of excited states in the topological insulator Bi_2Te_3. *Phys. Rev. B* **95**, 125405 (2017).
95. Abbate, M. et al. Probing depth of soft X-ray absorption spectroscopy measured in total-electron-yield mode. *Surf. Interface Anal*. **18**, 65–69 (1992).
96. Barla, A. et al. Design and performance of BOREAS, the beamline for resonant X-ray absorption and scattering experiments at the ALBA synchrotron light source. *J. Synchrotron Radiat*. **23**, 1507–1517 (2016).

Author contributions The bandstructure calculations were performed by M.M.O., M.B.-R., S.V.E. and A.Yu.V. The exchange-coupling constants calculations were performed by M.B.-R., Yu.M.K, M.M.O. and A.E. The paramagnons calculations were performed by A.E. The magnetic anisotropy studies were performed by M.M.O. The Monte Carlo simulations were performed by M.H. The topological invariant calculations were done by S.V.E. Tight-binding calculations were performed by I.P.R. and V.M.K. Crystals were grown by A.Z., A.I., Z.S.A. and M.B.B. X-ray diffraction measurements and structure determination were performed by A.Z. and I.R.A. The resistivity and Hall measurements, as well as contact preparation, were done by N.T.M., N.A.A. and V.N.Z. XMCD and resonant photoemission experiments were performed by R.C.V., T.R.F.P., C.H.M., K.K., S.S. and H.B. Magnetization experiments and their analysis were mainly performed by S.G., B.B. and A.U.B.W. with contributions by A.V.K. ARPES measurements were done by I.I.K., D.E., A.M.S., E.F.S., S.K., A.K., L.P., G.D.S., R.C.V., K.K., M.Ü., S.M. and H.B. The analysis of the ARPES data was done by I.I.K., D.E., R.C.V. and H.B. Spin-ARPES measurements were performed by I.I.K., D.E., A.M.S., F.F. and J.S.-B. ESR measurements were done by A.A. and V.K. The project was planned by M.M.O., A.I., H.B., A.M.S., N.T.M., F.R., P.M.E. and E.V.C. The supervision of the project was executed by E.V.C. All authors contributed to the discussion and manuscript editing. The paper was written by M.M.O. with contributions from A.I., H.B., V.K. and A.U.B.W.

Competing interests The authors declare no competing interests.

Additional information
Correspondence and requests for materials should be addressed to M.M.O. or E.V.C.
**Reprints and permissions information** is available at http://www.nature.com/reprints.
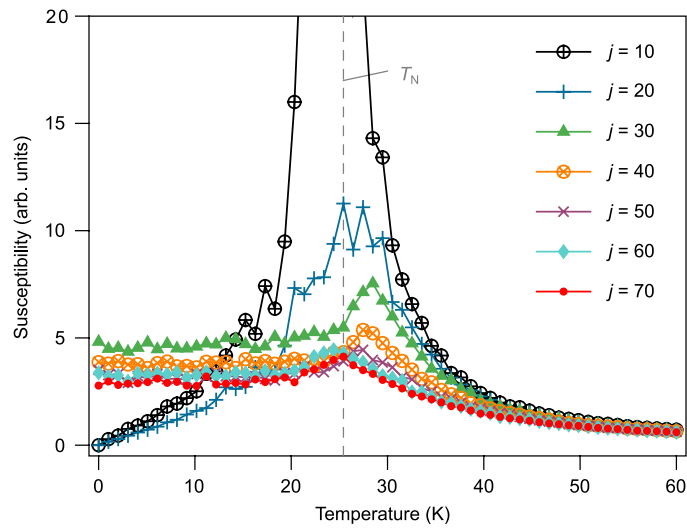
Extended Data Fig. 1 | Monte Carlo simulations for bulk MnBi$_2$Te$_4$. The temperature-dependent magnetic susceptibility of bulk MnBi$_2$Te$_4$ calculated for various numbers of magnetic shells j up to which the exchange-coupling constants $J_{i,j}$ were considered in the classical Heisenberg Hamiltonian. In increments of 10, results for 10–70 shells were calculated. The vertical dashed line shows the final Néel temperature of 25.4 K, estimated from the calculation for 70 shells. Note that the simulations revealed the onset of the AFM ground state only above 20 shells.

a

b

$E-E_F$ (eV)
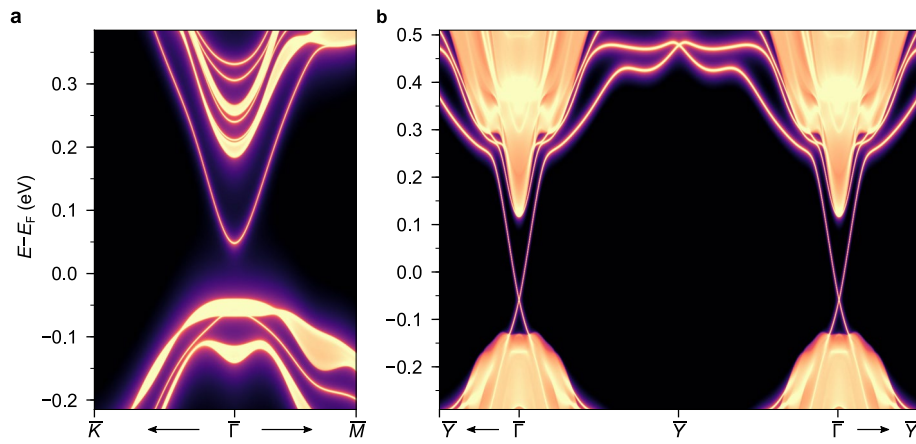
Extended Data Fig. 2 | Electronic structure of the *S*-breaking and *S*-preserving surfaces of MnBi₂Te₄. a, b, Surface electronic bandstructure of MnBi₂Te₄ calculated for the (0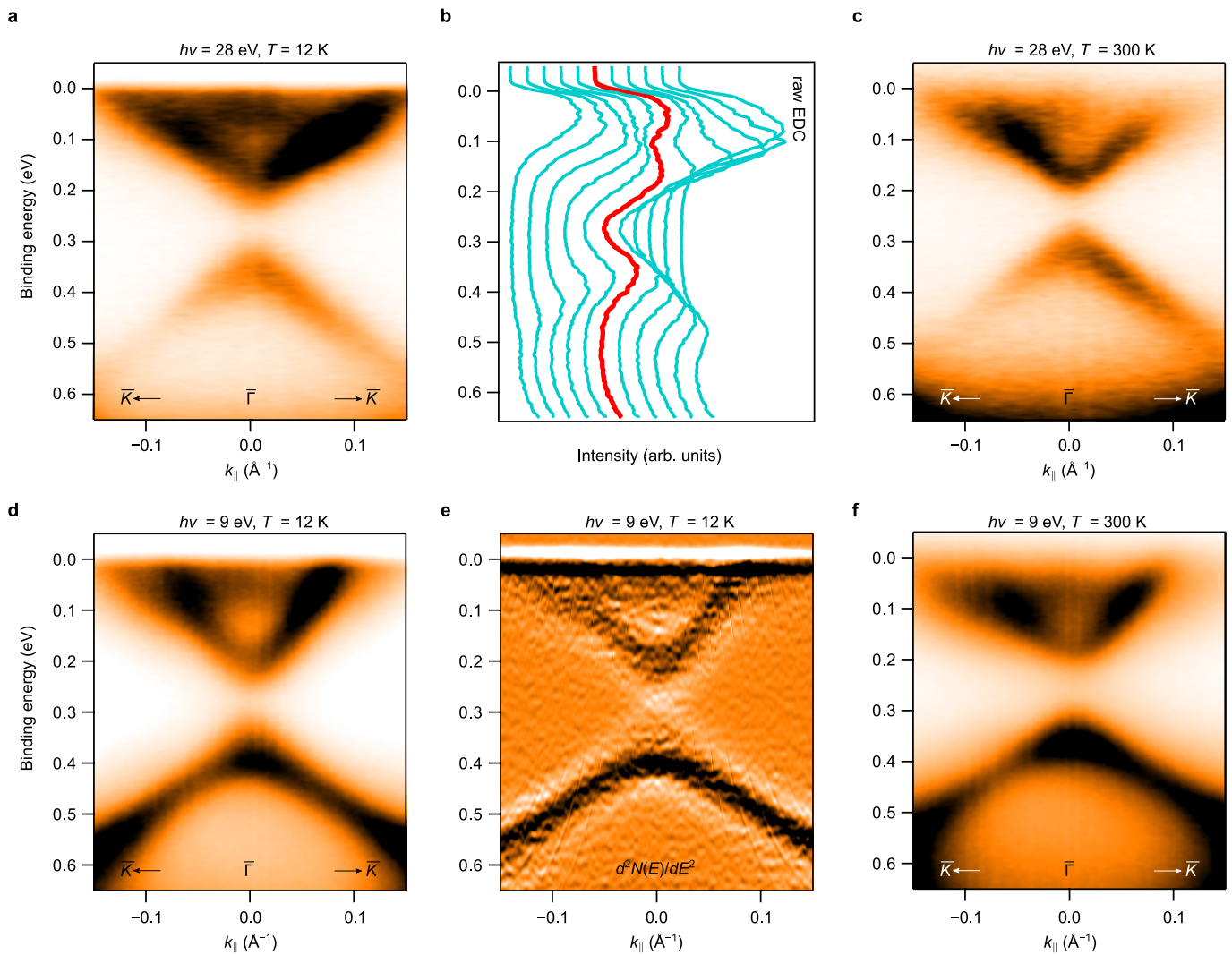001) (*S*-breaking; **a**), and (10Ī1) (*S*-preserving; **b**) terminations using the ab-initio-based tight-binding approach. The regions with a continuous spectrum correspond to the three-dimensional bulk states projected onto a two-dimensional Brillouin zone.
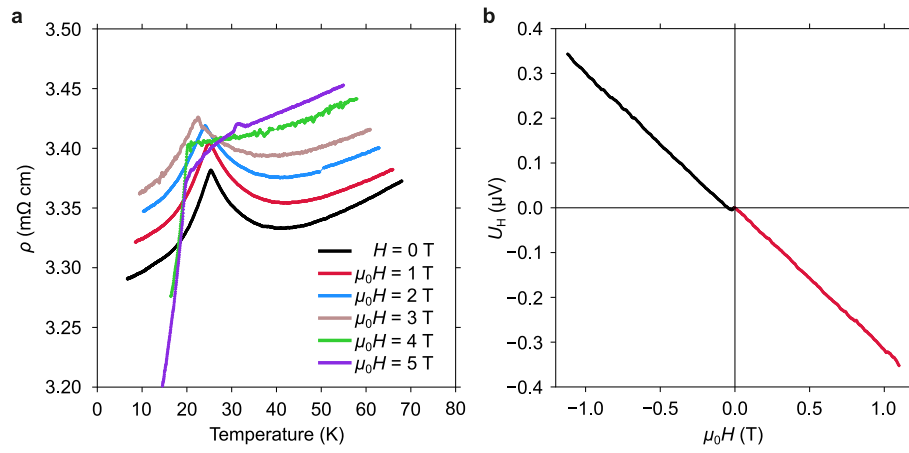
**Extended Data Fig. 3 | Resistivity and Hall measurements of bulk MnBi$_2$Te$_4$.** **a**, Temperature- and field-dependent resistivity data. **b**, Hall voltage as a function of the applied magnetic field for MnBi$_2$Te$_4$ at 5 K. The Hall-effect measurements unambiguously indicate n-type conductivity for our MnBi$_2$Te$_4$ samples that show a negative Hall voltage for positive values of the applied magnetic field. The estimated electron concentration and Hall mobility are around 2×10^{19} cm^{-3} and 100 cm^2 V^{-1} s^{-1}, respectively. The measurements were performed on B samples.

a $hv = 28$ eV, $T = 12$ K

b raw EDC

Intensity (arb. units)

c $hv = 28$ eV, $T = 300$ K

d $hv = 9$ eV, $T = 12$ K

e $hv = 9$ eV, $T = 12$ K

$d^2N(E)/dE^2$

f $hv = 9$ eV, $T = 300$ K

Extended Data Fig. 4 | D-sample ARPES. a, Dispersion of MnBi$_2$Te$_4$(0001) measured at 12 K with a photon energy of 28 eV. **b**, EDC representation of the data in **a**. The red curve marks the EDC at the $\overline{\Gamma}$-point. **c**, ARPES image acquired at 300 K ($hv = 28$ eV). **d**, Dispersion of MnBi$_2$Te$_4$(0001) measured at a temperature of 12 K with a photon energy of 9 eV (which is more bulk sensitive). **e**, The second derivative d$^2N(E)$/dE^2 of the data in **d**. **f**, ARPES image acquired at 300 K ($hv = 9$ eV). The measurements were performed on D samples.
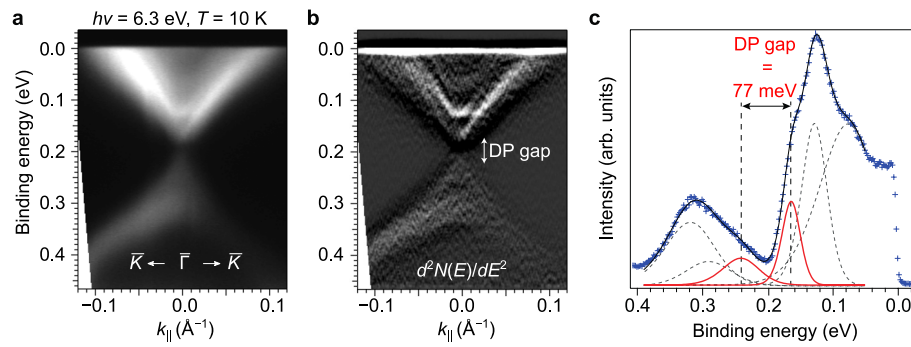
Extended Data Fig. 5 | Laser-based ARPES. a, ARPES map of $MnBi_2Te_4$ taken at 10 K with a photon energy of 6.3 eV. In this case, the photoelectrons have a kinetic energy of about 1.5 eV and, subsequently, a large mean free path in the sample, corresponding to a high bulk sensitivity of this experiment. **b**, The second derivative $d^2N(E)/dE^2$ of the data in **a**. **c**, Fitting results for the EDC spectrum at the $\bar{\Gamma}$-point. The raw data, the resulting fitting curve and its decomposition with Voigt peaks are shown by blue symbols, a black solid line and the grey dashed and red solid lines, respectively. Red (grey) lines indicate the peaks attributed to the gapped Dirac cone state (bulk bands). The measurements were performed on B samples.
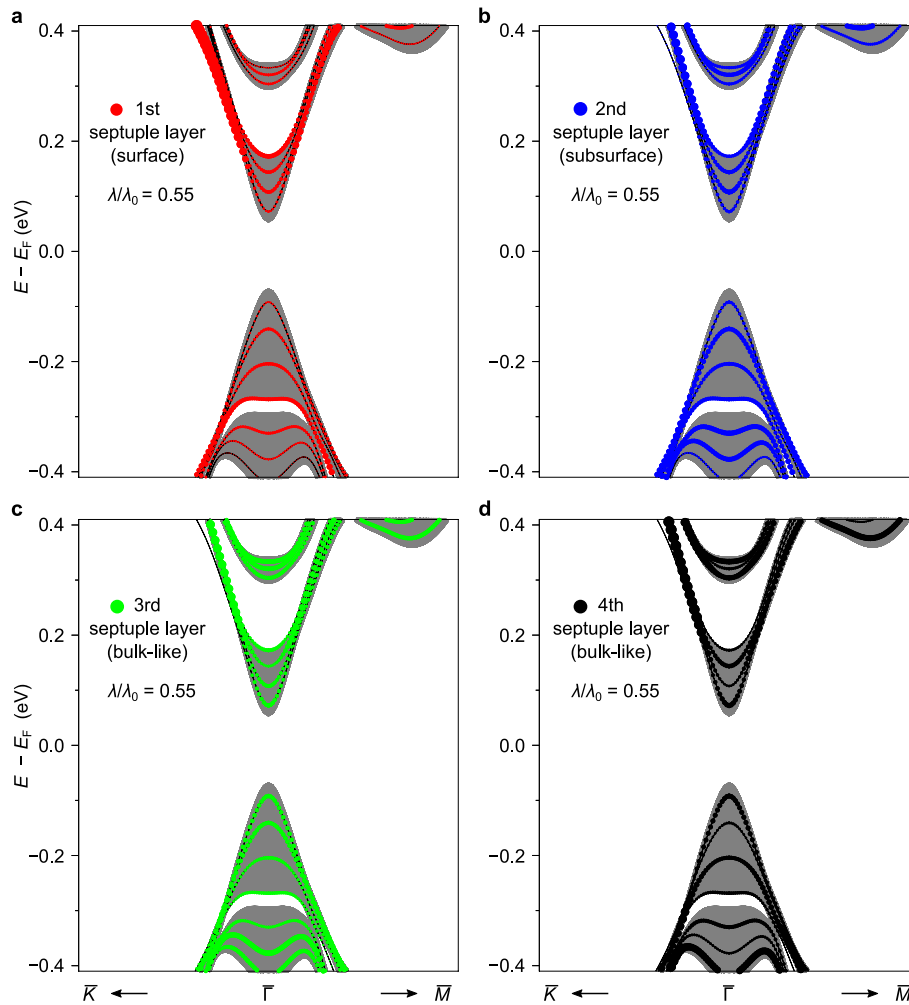
Extended Data Fig. 6 | Surface electronic structure of MnBi$_2$Te$_4$ in the artificial topologically trivial phase. Septuple-layer resolved (0001) surface electronic structure of MnBi$_2$Te$_4$ calculated for the SOC constant value $\lambda = 0.55\lambda_0$. The size of the colour circles that comprise the data reflects the state localization in a particular septuple-layer block of the eight-septuple-layer-thick slab. **a**, First septuple layer (that is, the surface layer; red). **b**, Second septuple layer (subsurface; blue). **c**, Third septuple layer (bulk-like; green).

d, Fourth septuple layer (bulk-like; black). The grey areas correspond to the bulk bandstructure projected onto the surface Brillouin zone. We see that near the $\overline{\Gamma}$-point there are (1) no surface states in the bulk bandgap and (2) no resonance states near the bandgap edges. The first quantum-well states of both the valence and conduction bands are strongly localized in the inner parts of the slab.
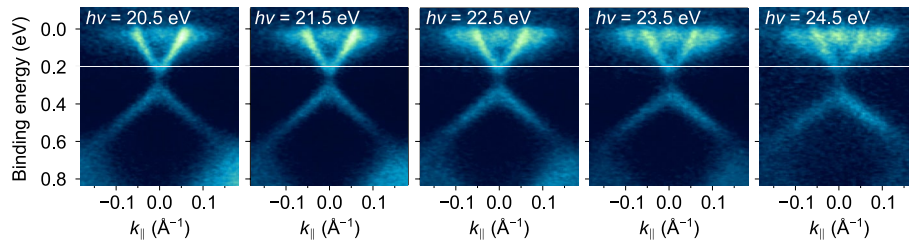
Extended Data Fig. 7 | Photon-energy-dependent ARPES data. Photon-energy-dependent ARPES data measured near the Brillouin zone centre along the $\overline{K}$–$\overline{\Gamma}$–$\overline{K}$ direction at a temperature of 18 K. Absence of any hv dependence confirms the surface-state character of the upper cone. The measurements were performed on D samples.
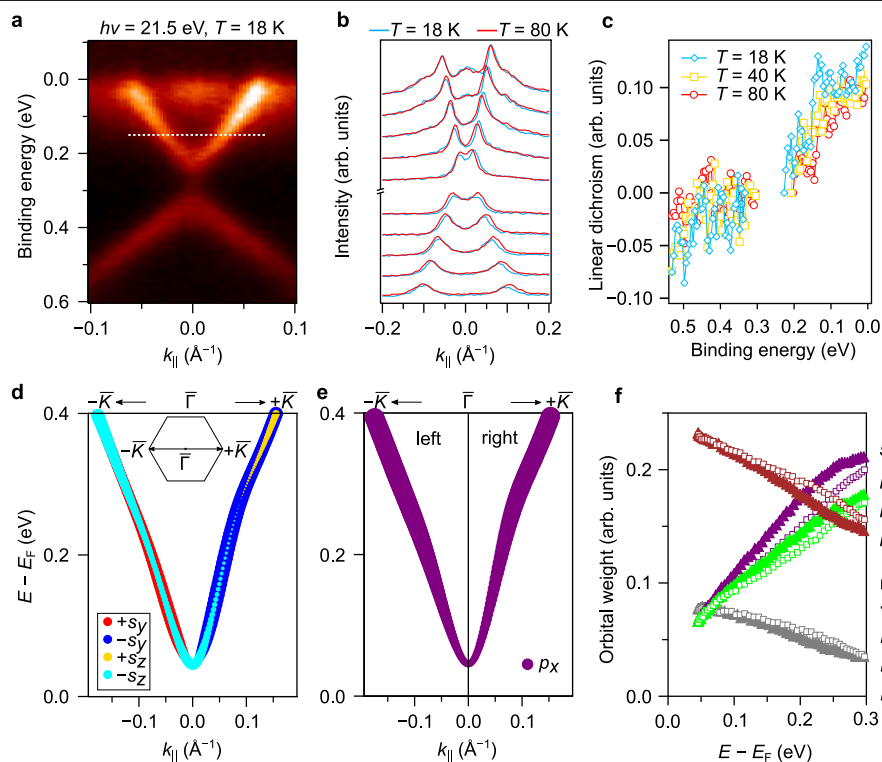
Extended Data Fig. 8 | Temperature-dependent linear dichroism in the Dirac cone photoemission intensity. a, Dispersion of $MnBi_2Te_4(0001)$ measured at 18 K with a photon energy of 21.5 eV and p-polarized light along the $\overline{K}-\overline{\Gamma}-\overline{K}$ direction. **b**, Momentum distribution curves representation of the data acquired at 18 K (blue) and 80 K (red). **c**, Linear dichroism ($I_{right}-I_{left}$), where I_{right} and I_{left} are the intensities of the right and left branches of the upper and lower cone corresponding to positive and negative $k_\parallel$, respectively. The measurements were performed on D samples. **d**, Upper part of the $MnBi_2Te_4(0001)$ gapped Dirac cone as calculated ab initio. The size of the coloured circles reflects the value and sign of the spin vector Cartesian projections, with red (blue) corresponding to the positive (negative) s_y

components (perpendicular to k_z), and yellow (cyan) to the out-of-plane components $+s_z$ ($-s_z$). **e**, As in **d**, but with the size of the purple circles reflecting the weight of the p_x orbitals of all Bi and Te atoms of the topmost septuple-layer block at each $k_\parallel$. Note that in **d**, **e** the bulk-like bands of the slab are omitted. The magnetic moment of the topmost Mn layer points towards vacuum, but in Fig. 1e and Extended Data Fig. 6 it points in the opposite direction. **f**, The weight of the s, p_x, p_y and p_z orbitals of all Bi and Te atoms of the topmost septuple-layer block for the left (triangles) and right (squares) branches as a function of energy. See Methods for more information on the dichroic ARPES measurements.
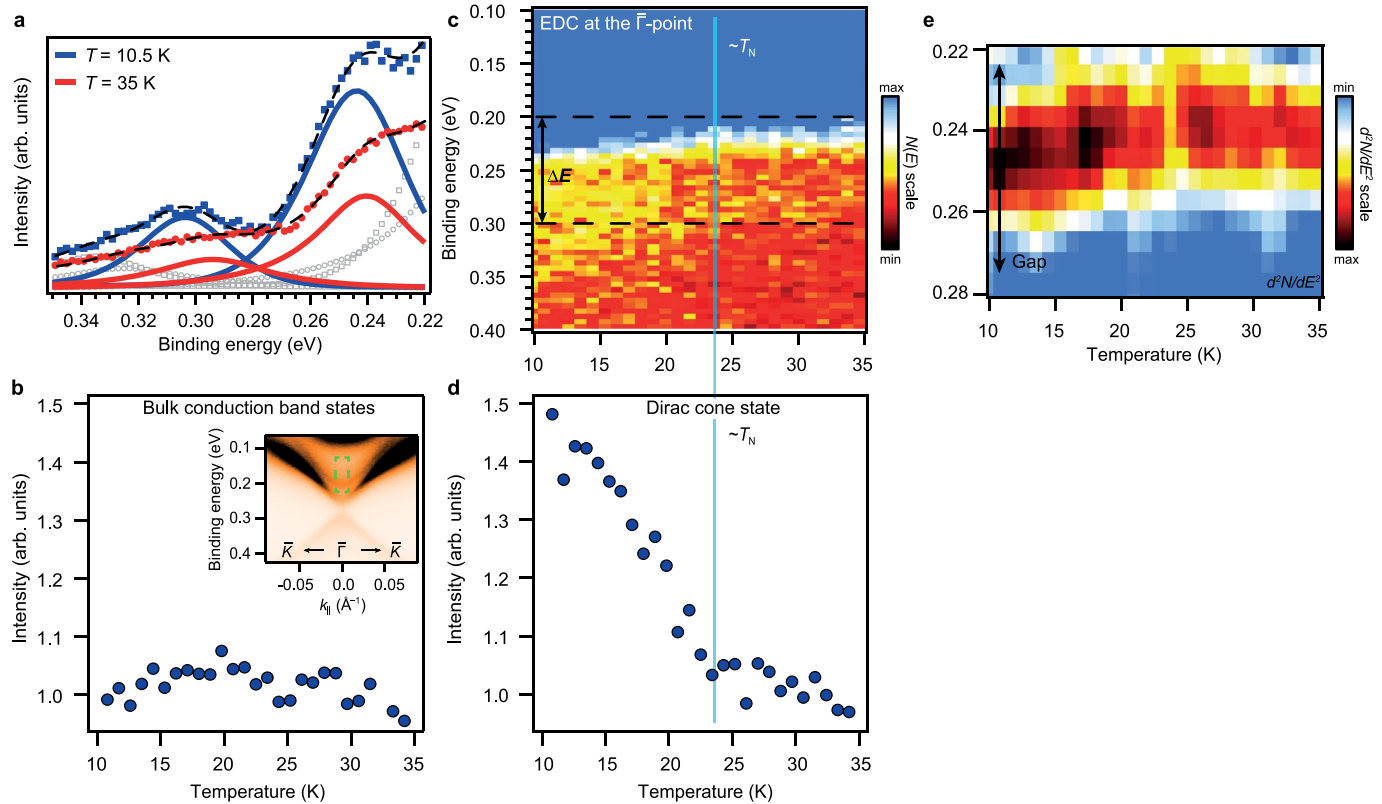
Extended Data Fig. 9 | Temperature-dependent laser ARPES measurements.
a, ARPES EDC profiles taken at the $\bar{\Gamma}$-point of $MnBi_2Te_4$(0001) at 10.5 K and 35 K. The raw data, resulting fitted curves, and their decompositions with Voigt peaks are shown by the coloured symbols, the black dashed lines, and the coloured lines and grey symbols, respectively. Red and blue lines (red circles and blue squares) indicate the peaks (EDCs) of the Dirac cone state at 35 K and 10.5 K, respectively. The peaks of the bulk bands at 35 K (10.5 K) are shown by grey circles (squares). **b**, Integrated intensity of the first two bulk conduction-band states (those analysed in detail in Extended Data Fig. 5c) as a function of temperature. Inset, The ARPES $MnBi_2Te_4$(0001) map measured with a laser photon energy of 6.4 eV and $T = 10.5$ K (as in Fig. 3d). The green rectangle marks the region of the map where the first two bulk conduction-band states are located. The average intensity in the shown temperature interval was set to 1. **c**, EDC profiles, $N(E)$, taken at the $\bar{\Gamma}$-point between 10 K and 35 K with a temperature step $\Delta T \approx 0.9$ K and two sweep directions (10 K → 35 K → 10 K).

Because the measurements upon heating and cooling reveal essentially the same behaviour, in **c** we show the data averaged over these two sets of the EDC profiles at each temperature point. Note that the data in **a** and the intensity dependencies on temperature in **b**–**d** were acquired from two different B samples, showing slightly different binding energy of the Dirac point gap centres (0.28 eV and 0.25 eV, respectively). **d**, Intensity integrated within the energy window ΔE marked by the dashed black lines in **c**. The average intensity in the plateau-like region above approximately 24 K was set to 1. ΔE contains both the lower and upper parts of the Dirac cone at the $\bar{\Gamma}$-point and corresponds to the energy interval in which the contribution of the cone is dominant and that of the bulk states is almost negligible. The vertical cyan line approximately shows the start of the intensity increase, which roughly corresponds to $T_N \approx 24$ K for $MnBi_2Te_4$. **e**, The second derivative, $d^2N(E)/dE^2$, of the EDC profiles in **c**, shown for a clearer visualization of the Dirac point gap behaviour.
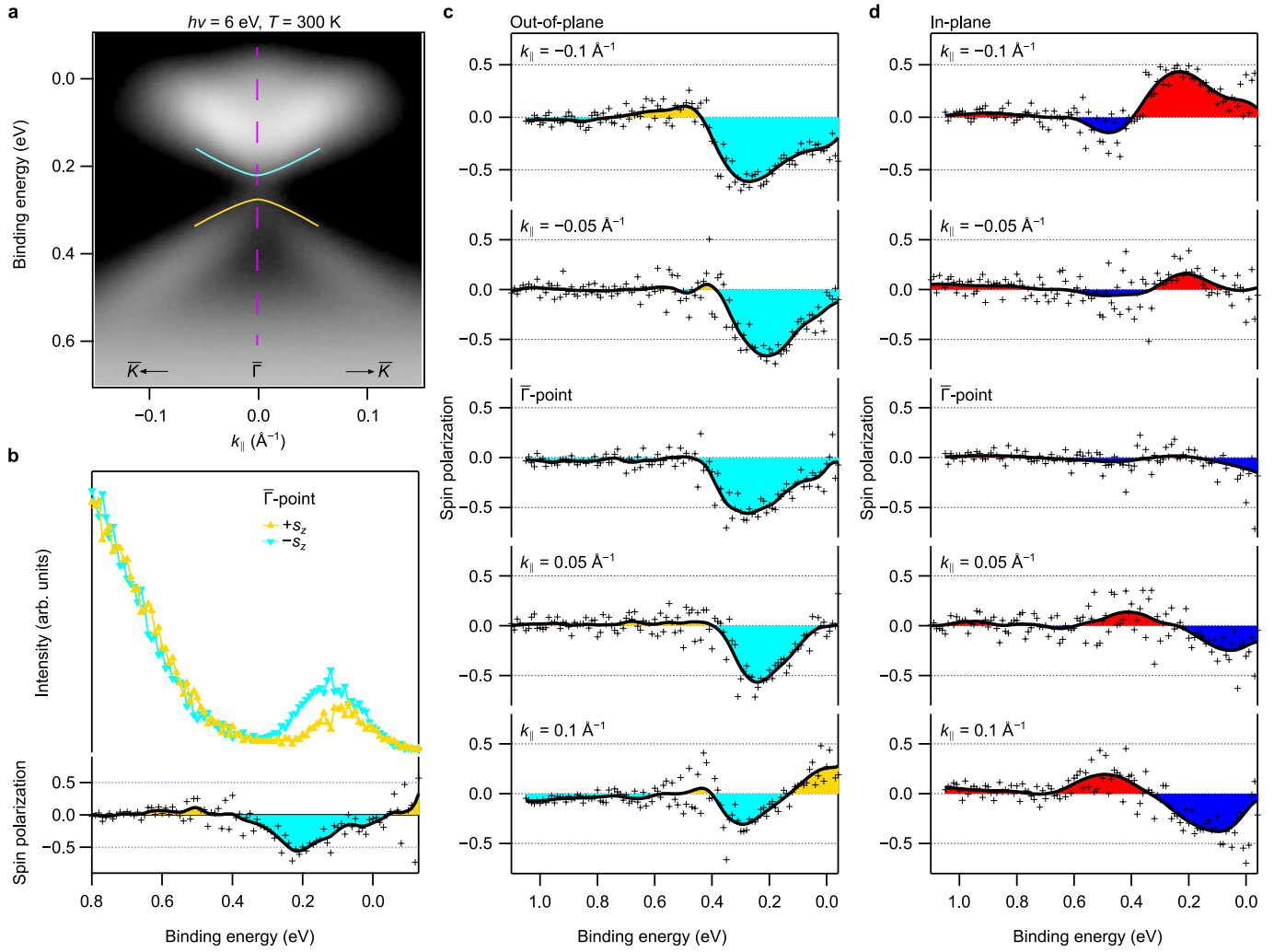
Extended Data Fig. 10 | Spin-resolved ARPES data. a, Spin-integrated ARPES spectrum taken at 6 eV photon energy along the $\overline{K}$–$\overline{\Gamma}$–$\overline{K}$ direction. Yellow and cyan curves show the location of the gapped TSS. **b**, Spin-resolved ARPES spectra taken at the $\overline{\Gamma}$-point with respect to the out-of-plane spin quantization axis. The out-of-plane spin polarization is shown below the corresponding spin-up and spin-down spectra. **c**, **d**, Measured out-of-plane (**c**) and in-plane (**d**) spin polarization at different momentum values. The in-plane spin polarization changes its sign with $k_\parallel$, as expected for the TSS. The change of the out-of-plane spin polarization sign at $k_\parallel = +0.1\,\text{Å}^{-1}$ near the Fermi level in **c** (bottom) is discussed in the Methods section 'Dichroic ARPES measurements'. The data in **a**, **b** and **c**, **d** were acquired on B and D samples, respectively. The measurements were performed at $T = 300$ K.